THE ASTROPHYSICAL JOURNAL, 377:349–364, 1991 August 20

THE PECULIAR VELOCITY FIELD IN THE HERCULES REGION

WOLFRAM FREUDLING[1]
National Astronomy and Ionosphere Center, Arecibo Observatory,[2] Arecibo, PR 00613

HUGO MARTEL
Center for Radiophysics and Space Research, Cornell University; and Département de Physique, Université de Montréal, C.P. 6128, Succ. A, Montréal, Que, Canada H3C 3J7

AND

MARTHA P. HAYNES
National Astronomy and Ionosphere Center and Center for Radiophysics and Space Research, Space Sciences Building, Cornell University, Ithaca, NY 14853

Received 1990 December 13; accepted 1991 February 25

ABSTRACT

We examine the three-dimensional distribution of galaxies in the Hercules region ($14^h \leq \alpha \leq 17^h$, $0° \leq \delta \leq 60°$) which contains the Hercules supercluster and an underdense region in front of the supercluster, the Hercules void. With the aid of the Tully-Fisher relation, we search for deviations from a smooth Hubble flow in that region.

New *I*-band CCD images have been obtained for 86 galaxies in the Hercules region. The sample was selected to minimize any bias in derived distances. The selection criteria are discussed in detail. Magnitudes and inclinations measured from those images are presented. The total magnitudes in combination with the inclination-corrected H I line widths are used to estimate redshift-independent distances. The comparison of those distances with the redshifts are used to estimate peculiar velocities of the galaxies.

A much bigger sample of 2165 galaxies for which only redshifts are known is used to model the gravitationally induced deviations from a smooth Hubble flow using the linear theory of gravitational perturbations. For the galaxies with redshift-independent distances, a comparison of the predicted velocities with those measured indicates a marginal correlation or a firm upper limit on the value for the density parameter Ω of 0.7.

Subject headings: cosmology — galaxies: clustering — galaxies: redshifts

1. INTRODUCTION

Recent new calibrations of the Tully-Fisher relation (hereafter TF relation) based on accurate magnitudes (Pierce & Tully 1988, hereafter PT) and large samples (Fouqué et al. 1990) have confirmed the reliability of the TF as a distance indicator. The fact that these works resulted in different values for the zero point of the TF relation does not affect its applicability to the measurement of relative distances and therefore peculiar velocities. Hence there are now two independent distance indicators in general use which can be applied to a large number of galaxies. The D_n-σ relation (Dressler et al. 1987) and the TF relation complement each other. Because of possible not recognized environmental dependence in either one or both of the relations (see, e.g., Silk 1989), such independent checks of measured peculiar velocities are important. Agreement of the measured quadrupole moment in the peculiar velocities obtained from both methods (Staveley-Smith & Davies 1989) strengthens the case for the reality of measured peculiar velocities. Similarly, the presence of the "Great Attractor" (hereafter GA) is now revealed with both the TF relation and the D_n-σ relation (Lynden-Bell et al. 1988; Dressler & Faber 1990). The partial success in reconstructing the local density distribution of galaxies from the measured peculiar velocities (Bertschinger & Dekel 1989) and the opposite approach to reconstruct the velocity field from the measured *IRAS* density distribution (Strauss & Davis 1988) can be seen as additional confirmation that the derived peculiar velocities are an actual measurement of gravitational induced velocities.

The peculiar velocity field has now been mapped over a large region of the sky, both in the general direction of the GA and more recently in the opposite direction (Willick 1990). Those wide-angle studies identified the overall streaming motion in the local universe. This work concentrates on a much smaller region on the sky, namely the Hercules region. The center of the Hercules region ($\alpha \approx 15^h30$, $\delta \approx 30°$) is almost perpendicular to the direction of the GA. The dominant streaming motion in the local universe as modeled by the GA should therefore have only a small impact on any streaming motion in the Hercules region. This region is therefore suitable to search for streaming motion on intermediate scale between those of Lynden-Bell et al. (1988) and models for the Virgocentric infall (e.g., Tully & Shaya 1984). At this length scale, the peculiar motion should map the gravitational potential. This application is discussed in detail in § 7.

Soon after redshift surveys revealed the importance of underdense regions or voids in the local universe, it was recognized that those voids present an opportunity to search for gravitationally induced streaming motion. In order to maximize the probability of detecting gravitational introduced peculiar motions around voids of galaxies, we chose the biggest void in the original redshift slice of the Center for Astrophysics (CfA) redshift survey (de Lapparent, Geller, & Huchra 1986) to search for deviations from a smooth Hubble flow using the TF

[1] Visiting Astronomer, Kitt Peak National Observatory, National Optical Astronomy Observatories, operated by AURA Inc., under contract with the National Science Foundation.

[2] The Arecibo Observatory is part of the National Astronomy and Ionosphere Center, which is operated by Cornell University under a cooperative agreement with the National Science Foundation.

relation. The far side of this void is delimited by the Hercules supercluster; hence, the void is referred to as the Hercules void and the surveyed region as the Hercules region.

The three-dimensional structure in the Hercules region is summarized in § 2. In § 3 we describe the sample of galaxies for which we obtained *I*-band CCD images. The data are presented in § 4, and the application of the TF relation to derive peculiar velocities is discussed in §§ 5 and 6. In §§ 7 and 8 we finally examine the measured peculiar velocities and compare them to a model of gravitationally induced streaming motion.

2. THE HERCULES REGION

The spatial structure in the Hercules region as determined from redshift surveys had been discussed in detail by Freudling, Haynes, & Giovanelli (1988, hereafter FHG) and Freudling (1990). The main results are briefly summarized here. Evidence of an underdense region at a redshift between 4900 km s^{-1} and 8900 km s^{-1} in the region $14^h \leq \alpha \leq 17^h$ and $+10° \leq \delta \leq +60°$ can be found from current redshift surveys. The northern part of the void is not well mapped; thus, it is not clear how far to the north the void extends. The redshift survey of Freudling (1990) in the northern part of the Hercules region shows that the void extends at least to a declination of $\delta = +60°$. The void is therefore strongly elongated in that direction. The most extensive boundary is the Hercules supercluster itself extending significantly beyond the volume of the void. The Hercules supercluster is part of the proposed structure nicknamed "Great Wall" (Geller & Huchra 1989). The void seems to be connected to the Coma void toward the west (Gregory, Tifft, & Moody 1988).

We compiled a sample of 2165 galaxies with measured redshifts in the region between $2.^\circ5 \leq \delta \leq 62.^\circ5$, $14^h \leq \alpha$ and $b \geq 40°$. This sample includes the compilation of redshifts by Huchra (1989), which he kindly made available to us, our own H I redshifts and redshifts from an optical survey in the northern part of the Hercules region carried out by Freudling (1990). The limits of this sample have been chosen to encompass the Hercules region and surroundings but to restrict the sample to a region where large number of redshifts are available. This sample is used in § 7 to construct a model of the expected streaming motion in the Hercules region.

The completeness of this sample has been estimated by counting the number of galaxies in the Hercules region listed in the Catalog of Galaxies and Clusters of Galaxies (Zwicky et al. 1961, hereafter CGCG) and by determining as a function of magnitude how many of them are contained in the redshift sample. The counts were performed separately in the five different regions with known differences in the selection effects, namely the declination range of the Arecibo Observatory, the region of the specially surveyed CGCG fields (see § 3), the region of the CfA redshift slice with $26.^\circ5 \leq \delta \leq 32.^\circ5$ (de Lapparent et al. 1986), the region of the optical redshift survey by Freudling (1990) with $50° \leq \delta \leq 60°$, and the remaining regions. All subsamples are complete to a blue magnitude of 14.5 because the area is covered by the CfA redshift survey (Huchra et al. 1982). The completeness drops sharply for fainter magnitudes in all regions but the CfA slice, for which the sample is complete to a magnitude of 15.5. The completeness of the whole sample is similar to the redshift sample considered in FHG (see Fig. 7 in FHG).

Figure 1 shows a histogram of the galaxy redshifts v in the region between $15^h30^m \leq \alpha \leq 16^h30^m$ and $20° \leq \delta \leq 40°$. This region has been chosen to show the projected inner part of the void. Superposed is the expected distribution $n(v)$ of a homogeneous sample with the same completeness, assuming a Schechter luminosity function with $M^* = -19.2$ and $\alpha = -1.1$ (de Lapparent, Geller, & Huchra 1989). Both the front and the back side of the void can clearly be seen. However, it also can be seen that the Hercules supercluster is a much higher overdensity than the front side of the void. This fact and the description of the void given at the beginning of this section make it clear that the void cannot simply be approximated by a sphere and makes our more complicated effort to model the expected streaming motion around the void necessary (see § 7).

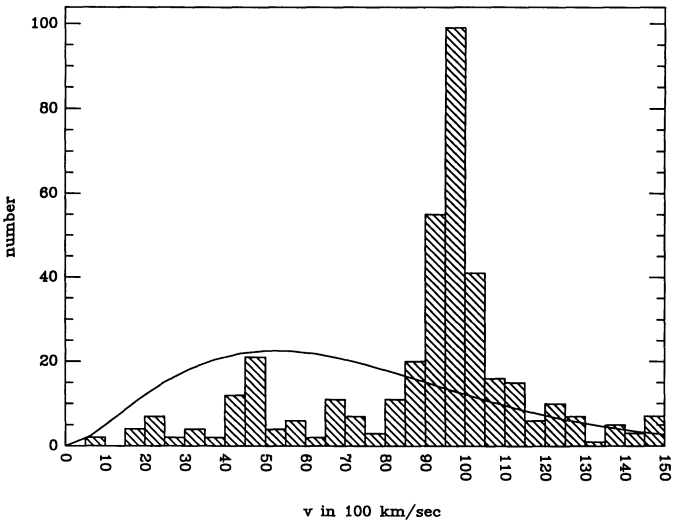

FIG. 1.—Redshift distribution in the center of the Hercules region ($15^h30^m \leq \alpha \leq 16^h30^m$, $20° \leq \delta \leq 40°$). The Hercules supercluster at a redshift of about 10,000 km s^{-1} and the void in front of the supercluster can easily be seen.

The estimated completeness of the redshift sample was also used to compute a weight,

$$w = \frac{v^2}{n(v)}, \tag{1}$$

where $n(v)$ is the number of galaxies expected at a redshift v in a homogeneous sample. The total weight per volume element can be considered as a relative mass density if light traces mass. From Figure 1 it becomes clear that by far the highest mass densities are found in the Hercules supercluster. The supercluster is therefore expected to dominate the streaming motion in the region (see § 7).

3. THE TULLY-FISHER SAMPLE

If the Hubble ratio is to be investigated as a function of redshift, it is important to select carefully a sample of "comparable" galaxies at various redshifts, i.e. the galaxies should only differ by redshift. Since there is *a priori* no reason to assume that the Tully-Fisher relation is linear, faint galaxies will not help us to predict the absolute magnitudes from the line widths of bright galaxies and vice versa. In magnitude-limited samples of galaxies, the average absolute magnitude depends on the distance and therefore any bias which depends on the absolute magnitude will introduce a nonreal velocity field. The bias arising from the shape of the luminosity function in magnitude-limited samples has been discussed in detail by

Teerikorpi (1990) and Bicknell (1991). In principle, it would be possible to correct the obtained raw magnitudes of galaxies in a magnitude-limited sample using formulaes provided by those authors for the case of a linear TF relation. In this paper we choose a different approach. We use the fact that any bias in the distance estimate influences the derivations of relative distances only if the bias is dependent on the positions of the galaxies. If there is a bias which affects all galaxies in the same way, relative distances can still be found by adjusting the zero point in the relation. The details are discussed in § 6. In this section we describe how the sample was selected so that any bias affects all galaxies in a similar way. The basic idea is to select galaxies by their absolute magnitude rather than the apparent magnitude. The bias discussed above in such a sample is similar for galaxies at various distances. The limitation of this method is our ability to select subsets of samples with similar brightness from existing magnitude limited catalogs. The selection of the sample used in this work started out with the selection of a sample for a H I survey in the Hercules supercluster. In the following the H I sample is first described, followed by a description of the final sample selected for the application of the TF relation.

As part of an extensive survey of the Hercules supercluster, we have previously obtained H I spectra for virtually all spiral galaxies listed in the Uppsala General Catalog (Nilson 1973, hereafter UGC) which are located between $0° \leq \delta \leq +38°$ and for late type spiral galaxies in selected fields of the CGCG in that region. The first part of this survey has been presented in FHG; the second part of this survey will be published in a separate paper (Freudling, Haynes, & Giovanelli 1991). This sample has been combined with H I measurements taken from the literature and with some measurements in the northern part of the Hercules region by Haynes & Giovanelli (1989). The total number of galaxies with measured H I parameters in the Hercules region is 888. Only the portion of the sample within the limits $0° \leq \delta \leq +38°$ is complete in the sense that more than 90% (785 out of 847) of all spiral galaxies listed in the UGC have been observed and detected. The CGCG fields with field numbers 105, 109, 134, 135, 136, 137, 138, 164, 165, 166, 167, 168, 191, 192, 193, 194, 195, 196, and 197 were selected for a deeper sample. They were chosen for their location on the projected position of the Hercules void. All galaxies listed in the CGCG in those fields were inspected with a magnifier on the Palomar Observatory Sky Survey (POSS) plates. They were included in the sample if they were judged to be late-type spirals and their position were measured on the POSS plates. A detailed description of the properties of this sample has to be deferred to the later paper.

From this data base of H I spectra, candidate galaxies for surface photometry were selected. The goal of the selection was to obtain a sample as homogeneous as possible for a wide range of redshifts, at least out to a redshift of 10,000 km s^{-1}, that is, the redshift of the far side of the Hercules void. The morphological type of late-type galaxies is more easily determined from the POSS plates (see FHG); late-type galaxies form a more homogeneous class than earlier types and their inclination can more easily be estimated because of the disk-dominated surface luminosity. Only galaxies of type Sbc to Scd were therefore included in the sample.

The absolute magnitude restriction presented us with a difficult choice. The faintest galaxies listed in the CGCG have an apparent blue magnitude of 15.7 mag. Some galaxies fainter than 15.7 mag are listed in the UGC and therefore in our H I sample, but those galaxies are low surface brightness objects and should not be included in constructing a homogeneous sample that approaches some limit in magnitude. The distance modulus to the Hercules supercluster is about 35 mag (all absolute magnitudes in this section are based on a Hubble constant of 100 km s^{-1} Mpc^{-1}) so no galaxies fainter than absolute blue magnitude -19.3 should be included in the sample. On the other hand, galaxies much brighter than -19.3 are scarce, and there are only a few at close distances. Also, bright galaxies which are close are too big to be imaged with the limited field of view of the telescope used for the imaging. Galaxies larger than about 3′ were difficult to image because of the necessity of sufficient blank sky in the image to subtract the background. Therefore only galaxies fainter than absolute blue magnitude -20.8 were selected; all of the selected galaxies had redshifts larger than 2000 km s^{-1}. These restrictions leave us with a rather small range of 1.5 mag. This is a disadvantage for the purpose of compiling a large enough sample of galaxies, but it minimizes the effects of biases in the derived distances (see § 6).

In addition to the absolute magnitude criterion, an inclination criterion was imposed for the selection of the sample. Higher inclinations are preferred for the application of the TF relation because of the necessary $(\sin i)^{-1}$ correction to the observed H I line widths. The exact criteria for the selection of the sample were the following:

1. The morphological type of the galaxies as judged from the visual inspection of glass copies of the Palomar Observatory Sky Survey (POSS) with a magnifier is Sbc to Scd.
2. The galaxies were isolated, i.e., no companions were found within 3′ to avoid possible confusion of the H I spectra within the antenna beam.
3. The absolute blue magnitude as computed from the blue magnitude listed in the CGCG and with a Hubble constant of 100 km s^{-1} Mpc^{-1} is between -19.3 and -20.8.
4. The axial ratio b/a as measured from the POSS plates is less than 0.8.

A candidate list was prepared from which the galaxies were selected at the telescope in such a way that all observations were made at low air mass.

The number of CCD frames obtained was larger than the number of images which could actually be reduced. Some images were discarded because they were overcrowded, their background was unusually uneven, or a bright star was included in the field. Another category of images not fully reduced were those for which the luminosity profile did not appear to follow an exponential decline in the outer part, making it impossible to apply the reduction procedure described in § 4. These rejections might introduce a slight bias against galaxies with very high inclinations, because those galaxies frequently are not elliptical in their projected shape, and their luminosity profile along the z-axis is frequently not exponential.

The total number of galaxies which could be fully reduced is 86. The properties of the resulting sample are shown in Figures 2 and 3. Figure 2 shows a histogram of the heliocentric redshift distribution. It can be seen that our sample is roughly evenly distributed throughout the covered redshift range between 2000 and 10,000 km s^{-1}, even at the position of the void at about 7000 km s^{-1}. In Figure 3 the absolute blue magnitude as a function of distance is plotted for the same sample of galaxies. The absolute magnitudes are computed with kinematic distances as listed in Table 1. It can be seen that

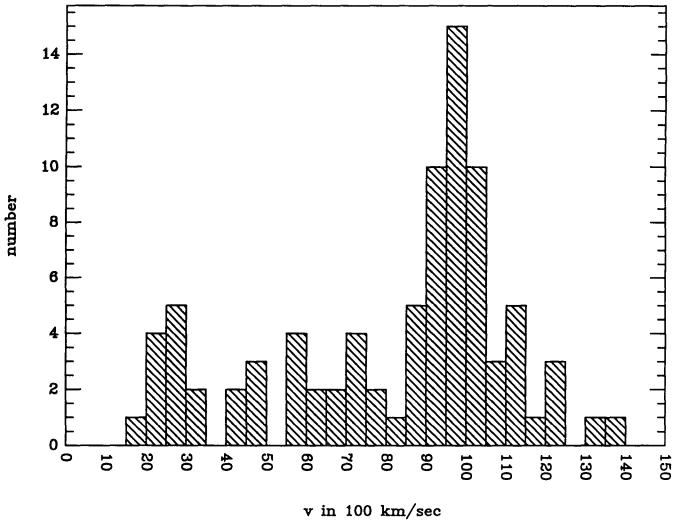

FIG. 2.—Redshift distribution of the Tully-Fisher sample. Note the relatively dense sampling even at the position of the void at about 7000 km s^{-1}.

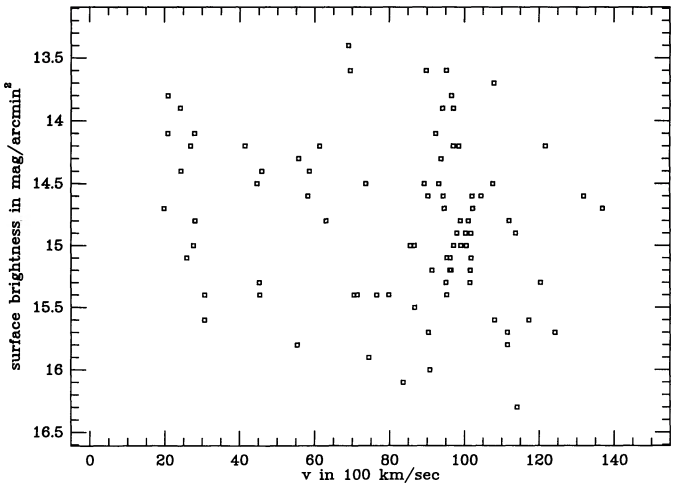

FIG. 4.—Surface brightness as a function of redshift for the Hercules sample. The surface brightness has been computed from corrected UGC diameters and corrected blue magnitudes as described in the text.

we successfully selected a similar absolute magnitude range for all redshifts.

One way to test whether the sample is homogeneous is to search for a distance dependence of the surface brightness. Figure 4 shows the surface brightness as computed from the blue magnitudes and UGC major axes as a function of redshift. For non–UGC galaxies we measured the major axes from the POSS plates. No redshift dependence is apparent, and this observation confirms that a homogeneous sample was selected.

4. OBSERVATIONS AND DATA REDUCTION

4.1. H I *Observations*

The H I line widths were measured from spectra taken with the Arecibo 305 m telescope and its 21 cm and 22 cm feeds. The dual circular feeds are characterized by a half-power beam width of about 3'.3. The 2048 channels of the autocorrelator were subdivided into four quadrants. The spacing between two channels was approximately 8 km s^{-1}, and the final velocity resolution after smoothing is about 15 km s^{-1}. The details of the observations and data reduction procedure of the H I sample are given in FHG.

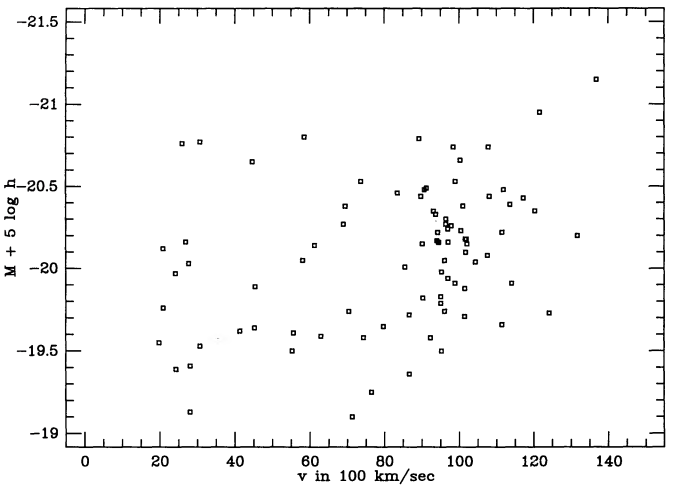

FIG. 3.—Absolute blue magnitudes of the Tully-Fisher sample as a function of redshift. The same absolute magnitudes range is sampled throughout the redshift range.

Earlier observations (before 1987) suffered from serious interference at higher redshifts from the San Juan airport radar (see FHG). In the fall of 1987, a radar blanker was installed at Arecibo observatory to reduce the effects of the interference of the San Juan airport radar. The radar blanker consists of a small antenna mounted on the platform of the telescope and directed toward San Juan. It is connected to a receiver which is tuned to the radar frequency of 1.350 GHz. The blanker takes advantage of the pulsed radar signal. A blanking pulse created by the blanker is fed into the autocorrelator and stops the integration temporarily when the radar pulse is on. The approximate radar pulse frequency is known to be 16.01 kHz, and the received signal is used to automatically adjust the frequency and phase of the blanking pulse. Approximately 20% of the integration time is lost when the radar blanker is in operation. But the interference environment improves dramatically for redshifts higher than about 11,000 km s^{-1}. Redshifts out to 14,000 km s^{-1} were detected. Some detections were made of lines close to the interference spikes listed in Table III of FHG which were previously hidden by the ringing of the spike. At the exact location of the spikes, however, some residual interference was left and only strong lines could be detected there even with the use of the radar blanker.

4.2. *I-Band Imaging*

In accordance with our goal of obtaining accurate surface photometry, *I*-band CCD frames for the Hercules sample were obtained with the No. 1 0.9 m telescope at the Kitt Peak National Observatory on seven clear nights in 1988 May, 1989 May, and 1990 May. The *I*-band filter of the so-called Mould filter set (Schoening 1988) was used in combination with the cooled RCA3 chip in 1988 and 1989 and the Tek chip in 1990. The optical system was arranged to give a telescope focal ratio of 7.5. Most images were exposed 600 s, and the sky background typically built up to about 5000 electrons, which corresponds to a surface brightness of the night sky of about 19.4

mag arcsec^{-1}. Since the readout noise of the chip is 42 electrons for the RCA3 chip and less for the TEK chip, the noise in the background is dominated by the quantum noise.

A plane was fitted to the overscan region and subtracted from each row in the image to remove the electrical DC offset. High spatial frequency variations in the DC offset were removed by subtracting the average of the bias frames.

After the debiasing procedure, the images were flattened by dividing by the average of the dome flats and the heavily smoothed sky flat obtained for each night. The heavy smoothing of the sky flats was necessary to avoid adding too much noise to the images, but this smoothing also removed high spatial frequency sensitivity variations from the sky flat. Therefore it was necessary to use the dome flats to remove the high-frequency variations from the images. The combined sky flats of all seven nights were smoothed and the residual from the smoothed image was subtracted from all images. This defringing procedure almost completely removed the fringes produced when the monochromatic sky background is reflected within the layers of the chip. Single pixels with counts differing by more than 5 times the rms of neighboring pixels were identified as cosmic ray events and removed by interpolation. This algorithm typically identified about 50 cosmic-ray events over the image. The total process of debiasing, defringing, and flattening of the images added about 10% to the noise of the background, most of it added by the defringing procedure.

The ultimate limit in the accuracy of the derived magnitudes is the estimate of the contribution of the sky background to the light within the elliptical apertures used to measure the brightness of the galaxy (see below). The average count per pixel contributed by the galaxy to the largest apertures used is typically 800 electrons, i.e., only a fraction of the contribution of the sky. A sky background of 5000 electrons will result in a background noise of roughly 70 electrons per pixel. This noise creates the potential of an error of several percent in the final magnitudes if the background is not carefully subtracted. The procedure for minimizing the impact of the uncertainty in the background removal on the derived total magnitudes is discussed below. Here we describe how the background was as carefully estimated as possible. The situation is aggravated by the fact that even after careful flattening, there was still a gradient of about 20% of the noise left in the background. We experimented with different schemes to estimate the background like fitting a plane to the edge of the image and interactively marking a region to be used for the estimate of the sky background. The best results were obtained with the following procedure, which was finally used on all images. First, a plane was fitted to the whole image. Then all 4 σ deviations from the fit were identified and a 10 pixel wide disk concentric with each 4 σ deviation was rejected. The next iteration was to fit a new plane to the remaining image and to reject again all 4 σ deviations and their adjacent pixels. The process was stopped after five iterations. Each image was then displayed with the rejected regions replaced by the last fit. This image was very carefully examined for any contamination by stars or remaining contribution from the galaxy which should have been removed by the 4 σ rejections. Special attention was paid to the edges of the removed galaxy to make sure that no light from the galaxy contributed to the fit of the plane. In cases of doubt, the pixel values of individual rows or columns were plotted as a function of the pixel number and inspected for any rise of the background estimate towards the edge of the galaxy. If an image passed this inspection, the last fit of the plane was subtracted. There are three adjustable parameters in this procedure: (1) the sigma clipping threshold, (2) the radius of the disk removed about each rejected pixel, and (3) the maximum number of iterations used. In about 80% of the images, the removal of stars and galaxies by this basic procedure was satisfying. In the remaining cases, any or all of the three parameters were varied until the surface fit passed the inspection. For several images, barely noticeable bad background subtractions were compared to the best background subtraction possible. Typically the difference was less than five electrons per pixel averaged over the whole galaxy.

Surface photometry was performed on the reduced and background subtracted images using the ISOPHOTE image reduction program package, which is part of the Space Telescope Science Data Analysis System (STSDAS), which runs under NOAO's Image Reduction and Analysis Facility (IRAF). Bright foreground stars and H II regions can interactively be masked with IRAF's task IMEDIT and are ignored in the further analysis by ISOPHOTE. The initial ellipse is specified as well. The contour fitting routine in ISOPHOTE then chooses successive larger major axes which are logarithmically spaced. It tries to fit isophotal ellipses to the intensity distribution for each of the major axes, varying the center and ellipticity of the ellipse. The variation of the counts around the marked center of the galaxy as a function of the angle from the major axis are analyzed. Then the first four coefficients of a Fourier expansion are fitted to it. If the Fourier coefficients are zero, then a perfect isophotal ellipse has been found. If the Fourier coefficients are above a given threshold, a new estimate of the parameters of the ellipse is computed from them. The routine is an implementation of the algorithm suggested by Jedrzejewski (1987). Masked regions can just be ignored in the fit of the Fourier coefficients; no interpolation is involved. The algorithm usually converges in less than 50 iterations, but in some cases, up to 100 iterations were needed. The contour fitting routine was set up to quit after 100 iterations if convergence was not obtained; this situation typically occurred only for outer ellipses where the average count along the ellipse was a small fraction of the noise in the background.

The counts of all pixels within each of the output ellipses were added. Pixels within the previously masked areas were assigned a value from a model of the surface distribution of the galaxy. This model was constructed from the previously fitted ellipses.

The luminosity profiles were used to fit an exponential disk to the part in the profile which is dominated by the disk. Total magnitudes were computed with the assumption that the exponential disk extends to infinity with constant ellipticity. This extrapolation typically adds about 0.02 mag to the last measured magnitude.

The main contribution to the uncertainty in the computed total and isophotal magnitudes is the uncertainty in the background and the calibration. The former is estimated as an additive constant of 10 electrons over the whole image, which is conservatively set to twice the previous estimate in the uncertainty of the background removal. This uncertainty in the background removal is by far the largest contribution to the total uncertainty in the derived magnitudes. The latter was obtained from the scatter in the aperture photometry of the calibration stars and is not worse than 0.02 mag. A third contribution is the uncertainty in the interpolation for isophotal magnitudes and extrapolation for the total magnitudes. It includes the scatter in the ellipticity of the ellipses fitted by

ISOPHOTE to the disk and the uncertainty in the fit of the disk luminosity profile. The points at a fainter surface magnitude in the luminosity profile are more affected by the uncertainty in the background removal, but including more points in the fit of the exponential disk will improve the computed confidence in the fit. The total magnitudes have been computed by adding the values of all pixels in each of the ellipses fitted by ISOPHOTE. Then lines were fitted to the exponential part of the disk varying the number of points used in the fit. The errors in the total magnitudes obtained from extrapolating each of the isophotal magnitudes to infinity were computed, including the impact of the uncertainty in the background on both the isophotal magnitude and the fit of the luminosity profile. Eventually the isophotal magnitude that resulted in the smallest error estimate if extrapolated to infinity was selected. In many cases this optimization led us to discard the outermost ellipses fitted by ISOPHOTE. Some images have been discarded because there were significant deviations from an exponential luminosity profile in the outer part, presumably because of insufficient background removal. Because the projected shape of highly inclined galaxies is not elliptical and the luminosity profile along the z-axis is not exponential, also many of the highly inclined galaxies could not be fully reduced.

The average ellipticity measured in the exponential part of the luminosity profile was used as an estimate of the ellipticity of the disk. In most cases the ellipticity of the fitted outer ellipses did not systematically decrease or increase along the major axis and the scatter of the ellipticities was used to estimate its uncertainty. If the ellipticity as a function of radial distance along the major axis had a slope larger than the scatter, then half the range of the measured ellipticity was used as an error estimate.

The inclinations of the galaxies have been estimated from the ellipticity of the disk assuming an intrinsic axial ratio r_0 of 0.2. The inclination has been computed using the standard relation

$$\cos^2 i = \frac{r^2 - r_0^2}{1 - r_0^2}, \qquad (2)$$

where r is the ratio of the measured minor axis to the major axis. The inclination was set to 90° for galaxies with $r < 0.2$.

Table 1 lists both the I-band CCD parameters obtained from the images and the parameters measured from the H I spectra. All error estimates are 1 σ estimates. Columns of Table 1 have the following meanings:

Column (1).—Name of galaxy. Line 1: UGC numbers or CGCG designation of the galaxy. CGCG designations are listed only if the galaxy is not listed in the UGC. Line 2: NGC or IC number if available.

Column (2).—The 1950.0 equatorial coordinates of the galaxy measured from overlays on the Palomar Observatory Sky Survey (POSS) prints to an accuracy of about 0.'1.

Column (3).—Line 1: Total I-magnitudes as measured from the luminosity within one of the outer isophotal ellipses and extrapolated to a major axis of infinity. The extrapolation assumes that the exponential disk extends to infinity with constant ellipticity. The outermost ellipse from which on the luminosity was extrapolated was chosen to minimize the error estimate in the total magnitude. Line 2: 1 σ error estimate for the total I-band magnitude. The error estimate includes the uncertainty in the background removal, the uncertainty in the extrapolated luminosity profile, and the uncertainty in the zero point for the night.

Column (4).—The total magnitude corrected for galactic and internal absorption and bandpass as described in § 5.

Column (5).—Line 1: Ellipticity of the disk of the galaxy. The ellipticity is the average of the ellipticities in the exponential part of the luminosity profile. Line 2: 1 σ error estimate in the ellipticity.

Column (6).—Line 1: Inclination estimate in degrees computed from the ellipticity listed in column (4) with the assumption of an intrinsic axial ratio of 0.2. Line 2: Error estimate in the inclination in degrees computed from the uncertainty in the ellipticity. No allowance is made for the uncertainty in our knowledge of the intrinsic axial ratio.

Column (7).—Line 1: Heliocentric velocity measured from H I profile as described in FHG. Line 2: Error estimate for heliocentric velocity computed as discussed in FHG.

Column (8).—Line 1: Line width measured from H I profile with the "0.5 MEAN" algorithm as discussed in FHG. Line 2: Error estimate for H I line width computed as discussed in FHG.

Column (9).—Line 1: H I line width corrected for redshift and inclination. Line 2: Error estimate for line width. The error is the combined error estimates in inclination (col. [6]) and measurement uncertainty in width (col. ([8]).

The total number of galaxies for which we were able to obtain surface photometry is 86. For a total of 13 galaxies, we obtained more than one image. Some of the subsequent images were taken during the same night, but most images were taken at different nights and pairs of images cover all observing periods and CCD chips used. The rms of the difference between the individual magnitudes divided by the combined error estimates of the images involved is 0.95. We therefore believe that the error estimates for the total magnitudes as listed in Table 1 reflect accurately the internal errors. The external error can be estimated from the four galaxies in this sample which are in common with PT's sample. The four galaxies are UGC 7600, UGC 7279, UGC 7352, and UGC 7822. The average difference between PT's total magnitudes and the ones presented here is −0.02 mag, and the rms difference is 0.10 mag. Assuming that PT's magnitudes and ours are equally accurate, we then find an accuracy of 0.07 mag. The error estimates of the four galaxies in Table 1 are higher than that. Those estimates might therefore be conservative for large galaxies.

5. T-F RELATION

We have followed Pierce & Tully in the adopted correction schemes for the magnitudes and widths, because that work is the only one so far which includes a zero point for the I-band TF relation. We note, however, that the zero point is based only on a single galaxy (NGC 2403) and that the purpose of this study is not the derivation of a value for the Hubble constant.

We first turn to the H I line width and its corrections. The H I line widths published by various authors have been measured by applying different algorithms to the raw spectra. The various algorithms result in systematically different values for line widths derived from the same spectra. Commonly used algorithms include ones that measure the line width at flux levels corresponding to certain percentages of the peak or mean flux of the emission line. Bicay & Giovanelli (1986) have investigated five different algorithms used to extract both the line width and the systemic redshifts from H I spectra. They found that their "0.5 MEAN" algorithm is the least vulnerable to random errors and at the same time is robust against large

TABLE 1

GALAXY PARAMETERS

name	ra dec	I ±	I_{corr}	ϵ ±	i ±	v_{hel} ±	w ±	w_{corr} ±
(1)	(2)	(3)	(4)	(5)	(6)	(7)	(8)	(9)
U8185	13h03m23.8s	12.56	12.50	0.330	49.3	2533	237	322
N4961	+28°00′09″	0.04		0.015	1.2	4	4	6
U8337	13h13m51.4s	12.18	12.10	0.467	59.7	5591	363	424
N5056	+31°12′47″	0.10		0.026	1.9	4	5	9
U8356	13h15m10.5s	12.73	12.68	0.358	51.5	5550	288	373
N5065	+31°21′25″	0.05		0.013	1.0	4	5	6
U8555	13h32m13.6s	12.17	12.14	0.292	46.1	7068	371	517
I 900	+09°35′35″	0.05		0.008	0.7	4	5	6
U8700	13h43m11.6s	10.69	10.39	0.736	79.9	2579	479	482
N5290	+41°57′55″	0.04		0.014	1.3	15	30	30
U8709	13h44m19.0s	10.80	10.57	0.689	75.9	2404	422	432
N5297	+44°07′22″	0.04		0.019	1.5	15	30	31
U8753	13h48m26.0s	13.79	13.59	0.681	75.3	9185	391	403
	+25°26′19″	0.11		0.023	1.8	7	11	11
U8873	13h54m56.0s	13.15	12.94	0.693	76.2	8891	538	549
	+24°30′00″	0.04		0.046	3.7	14	28	29
U8887	13h55m41.9s	13.63	13.52	0.531	64.3	8303	429	474
	+20°38′32″	0.06		0.004	0.3	12	23	23
U8966	14h00m59.9s	14.16	14.08	0.474	60.2	7379	268	312
	+07°01′00″	0.06		0.032	2.3	33	76	77
U8998	14h02m11.6s	14.85	14.64	0.692	76.2	9922	350	359
	+26°02′02″	0.08		0.023	1.8	14	27	27
U8996	14h02m18.4s	13.84	13.45	0.808	90.0	7184	432	432
	+14°31′06″	0.05		0.016	1.7	5	9	9
U9019	14h03m53.5s	13.82	13.73	0.507	62.6	11124	437	486
	+20°22′53″	0.06		0.028	2.0	5	6	10
U9044	14h06m37.2s	12.94	12.86	0.454	58.8	5314	342	404
	+14°33′00″	0.04		0.006	0.4	15	30	30
U9048	14h06m42.5s	13.31	12.99	0.758	82.0	10601	534	531
	+33°46′13″	0.05		0.006	0.6	16	32	32
U9101	14h11m00.9s	12.68	12.59	0.480	60.7	5306	398	460
	+27°14′30″	0.06		0.009	0.7	4	5	5
U9127	14h13m27.4s	11.02	10.62	0.868	90.0	2878	590	584
N5529	+36°27′29″	0.10		0.012	0.0	15	30	30
U9134	14h14m08.0s	13.86	13.81	0.425	56.6	11157	332	395
	+10°12′39″	0.14		0.011	0.8	4	5	6
U9259	14h25m02.6s	13.22	13.15	0.439	57.7	8429	363	430
	+11°15′59″	0.08		0.001	0.1	28	62	62
U9270	14h25m37.2s	12.41	12.23	0.633	71.7	2658	230	240
N5630	+41°28′51″	0.05		0.005	0.4	15	30	30
192-028	14h26m26.1s	14.10	14.02	0.473	60.2	8803	280	324
	+36°42′40″	0.06		0.018	1.3	8	12	13
192-035	14h29m18.4s	13.77	13.64	0.548	65.6	6766	277	308
	+33°26′52″	0.05		0.096	6.9	4	5	16
U9375	14h31m41.4s	13.86	13.53	0.764	82.7	9421	490	489
	+28°37′12″	0.05		0.009	1.0	33	77	77
U9416	14h35m09.2s	11.04	10.68	0.748	81.0	1749	316	328
N5690	+02°30′13″	0.06		0.025	2.5	4	4	5
164-007	14h36m52.2s	13.85	13.80	0.382	53.4	10256	301	374
	+31°01′46″	0.04		0.003	0.2	10	19	19
U9490	14h41m13.3s	13.56	13.22	0.769	83.2	10936	464	461
	+11°21′19″	0.13		0.016	1.9	9	16	17
U9510	14h43m40.0s	13.73	13.50	0.696	76.5	8495	449	460
	+32°50′13″	0.05		0.013	1.0	24	52	52
U9533	14h45m59.0s	13.39	13.12	0.727	79.1	8819	456	462
	+14°09′53″	0.05		0.004	0.4	15	30	30
U9548	14h47m56.1s	13.71	13.64	0.484	61.0	10998	476	537
	+16°55′32″	0.09		0.037	2.7	15	29	31
U9558	14h48m51.1s	13.32	13.28	0.366	52.1	13487	446	554
	+17°23′34″	0.10		0.015	1.2	9	15	17
U9593	14h52m30.8s	13.26	13.17	0.485	61.0	6108	308	356
I1075	+18°18′27″	0.09		0.072	5.2	5	6	17
164-052	14h57m31.4s	14.41	14.34	0.414	55.8	9077	337	407
	+29°08′59″	0.13		0.006	0.5	4	5	5
U9646	14h57m32.5s	15.28	14.87	0.839	90.0	9627	304	304
	+27°31′07″	0.07		0.020	0.0	5	7	7
134-071	15h00m56.4s	14.44	14.04	0.793	86.9	11989	478	471
	+21°44′20″	0.03		0.004	1.0	5	6	6
U9677	15h01m28.1s	13.52	13.17	0.761	82.3	11553	695	685
	+22°53′39″	0.04		0.002	0.2	19	38	38
U9701	15h03m32.5s	13.88	13.83	0.407	55.3	10019	307	373
	+31°21′20″	0.17		0.031	2.3	9	15	18
165-017	15h03m43.2s	14.70	14.67	0.330	49.3	13031	262	343
	+31°52′25″	0.08		0.016	1.3	5	6	8
U9712	15h04m24.0s	13.55	13.17	0.763	82.5	6860	366	371
	+12°45′59″	0.06		0.021	2.4	6	9	10
135-037	15h13m02.9s	13.98	13.89	0.487	61.2	10068	364	413
	+25°11′13″	0.12		0.038	2.8	17	34	36
U9789	15h13m14.8s	10.76	10.54	0.657	73.5	2589	499	527
N5899	+42°14′01″	0.03		0.030	2.3	5	7	9
135-039	15h14m08.7s	13.97	13.70	0.717	78.2	6746	273	282
	+25°03′13″	0.05		0.011	0.9	6	10	10
U9841	15h23m17.2s	12.30	11.85	0.813	90.0	4390	433	437
	+18°27′16″	0.03		0.002	0.0	5	8	8
U9843	15h23m25.7s	13.95	13.82	0.500	62.1	11894	344	385
	+20°57′46″	0.16		0.011	0.8	8	13	13
U9860	15h25m16.1s	14.13	13.91	0.699	76.7	9493	344	353
	+31°09′26″	0.15		0.028	2.3	9	16	16
U9916	15h32m59.4s	14.53	14.24	0.713	77.9	9332	365	372
	+24°15′53″	0.08		0.005	0.4	8	14	14
U9921	15h33m34.5s	14.17	13.98	0.622	70.9	9928	381	401
	+26°29′53″	0.05		0.006	0.4	12	24	24
U9926	15h34m14.1s	10.39	10.31	0.296	46.5	1957	358	505
N5962	+16°46′23″	0.03		0.007	0.6	4	4	6
U9943	15h36m08.1s	10.47	10.38	0.412	55.6	1957	331	410
N5970	+12°20′53″	0.02		0.006	0.5	4	4	5
166-024	15h36m37.8s	14.78	14.71	0.386	53.7	9778	278	345
	+29°35′27″	0.08		0.010	0.8	5	7	8
U9978	15h39m44.2s	14.35	14.20	0.590	68.6	7836	295	319
	+06°48′19″	0.19		0.023	1.7	6	9	9
U10011	15h43m14.5s	13.57	13.37	0.620	70.7	9995	445	467
	+25°36′00″	0.03		0.006	0.4	19	39	39
166-055	15h44m31.5s	13.07	12.94	0.540	65.0	9607	541	590
	+32°16′34″	0.05		0.007	0.5	16	31	31
U10074	15h50m39.0s	13.55	13.47	0.338	49.9	9613	351	457
	+24°32′20″	0.07		0.015	1.2	15	31	31
U10094	15h53m37.9s	13.98	13.53	0.819	90.0	9752	499	494
	+24°38′09″	0.11		0.016	0.0	25	54	54
108-018	15h55m20.4s	13.99	13.89	0.490	61.4	9414	316	360
	+18°10′07″	0.01		0.007	0.5	15	30	30
U10121	15h57m31.0s	12.82	12.76	0.361	51.7	8830	389	475
	+18°56′27″	0.05		0.069	5.4	20	41	49
108-037	15h57m41.0s	13.33	13.13	0.660	73.7	10099	598	597
	+15°43′53″	0.03		0.028	2.1	10	19	20
108-043	15h58m26.1s	14.28	14.25	0.333	49.5	10660	270	337
	+16°51′20″	0.08		0.017	1.4	24	52	53
137-028	16h02m28.8s	13.35	13.17	0.607	69.8	9568	514	542
	+25°19′27″	0.02		0.058	4.2	26	56	57
U10196	16h03m41.6s	11.44	11.25	0.573	67.4	4440	484	528
N6060	+21°37′07″	0.05		0.027	1.9	4	4	8
U10227	16h07m07.9s	12.75	12.35	0.857	90.0	9022	636	628
	+36°44′13″	0.08		0.010	0.0	13	25	25
U10233	16h07m42.7s	13.94	13.50	0.830	90.0	9822	472	467
	+22°44′33″	0.06		0.012	0.0	13	25	25
U10236	16h07m55.9s	12.83	12.63	0.616	70.5	9951	561	587
	+22°46′46″	0.03		0.036	2.6	36	84	85
196-007	16h11m46.9s	13.90	13.72	0.608	69.9	9643	462	488
	+34°24′53″	0.06		0.003	0.2	9	18	18
U10305	16h13m57.8s	14.60	14.41	0.651	73.0	9469	307	321
	+31°48′46″	0.05		0.015	1.1	9	15	15
U10355	16h20m02.3s	14.68	14.25	0.789	86.1	10104	419	416
	+13°58′13″	0.05		0.004	0.7	13	25	25
109-027	16h28m37.4s	13.60	13.48	0.446	58.2	10734	358	418
	+20°27′39″	0.04		0.021	1.6	8	14	15
U10439	16h30m09.4s	10.66	10.51	0.426	56.7	2370	392	478
N6181	+19°55′48″	0.04		0.081	6.1	4	4	28
U10475	16h35m28.6s	13.94	13.76	0.461	59.3	9480	411	475
	+07°39′39″	0.02		0.017	1.2	5	8	9
U10498	16h37m23.0s	15.66	15.36	0.743	80.5	12391	390	390
	+29°27′52″	0.15		0.050	5.3	20	41	41
197-006	16h39m32.6s	13.88	13.77	0.402	54.9	9393	326	398
	+33°26′39″	0.03		0.068	5.2	5	6	22
168-032	16h43m15.6s	14.49	14.24	0.661	73.8	9362	308	321
	+31°23′39″	0.03		0.021	1.6	11	20	20
U10545	16h45m03.3s	13.36	13.22	0.580	67.9	9307	410	440
	+34°29′52″	0.03		0.051	3.7	36	83	84
U10550	16h45m23.9s	13.97	13.61	0.769	83.2	9032	366	368
	+40°13′00″	0.05		0.003	0.4	6	9	9
U10582	16h49m06.4s	14.16	13.91	0.673	74.7	11137	395	405
	+24°01′59″	0.05		0.007	0.5	21	45	45
U10615	16h54m21.2s	13.89	13.75	0.589	68.5	9512	426	455
	+34°54′46″	0.11		0.027	1.9	17	34	35
U10661	16h59m32.8s	13.78	13.41	0.742	80.4	10151	570	570
	+28°00′33″	0.03		0.043	4.3	24	51	52
U10685	17h02m31.3s	13.50	13.22	0.646	72.7	9643	444	461
	+12°59′19″	0.04		0.006	0.4	5	7	7
U10723	17h07m00.0s	12.02	11.96	0.406	55.2	8381	539	651
N6301	+42°24′00″	0.05		0.009	0.7	17	34	34
U10807	17h17m40.5s	12.31	12.12	0.441	57.8	6146	386	441
N6347	+16°42′36″	0.05		0.013	1.0	17	35	35
U10893	17h30m25.7s	11.16	10.91	0.538	64.8	3115	420	454
N6389	+16°26′16″	0.05		0.022	1.6	4	4	7
U10934	17h37m40.4s	11.81	11.63	0.563	66.6	2487	329	366
N6434	+72°07′03″	0.05		0.053	3.8	5	6	12
U10972	17h44m21.6s	12.49	12.04	0.742	80.4	4651	416	426
	+26°33′40″	0.03		0.007	0.7	4	5	5
U11001	17h47m56.9s	12.59	12.32	0.623	71.0	4211	327	351
	+14°18′00″	0.06		0.027	2.0	8	12	13
U11091	17h58m55.7s	13.77	13.66	0.318	48.3	7216	293	396
	+35°00′33″	0.06		0.012	1.0	9	14	15
U11429	19h19m22.0s	11.12	10.88	0.521	63.6	4638	546	612
N6792	+43°02′14″	0.04		0.069	5.0	6	9	25

NOTE.—See text for explanation of columns.

errors caused by highly asymmetrical profiles. The 0.5 MEAN algorithm measures the line width at a flux level of 50% of the mean line flux. It was this finding that led us to use this algorithm to measure line width and redshifts. PT used line widths measured with a "0.2 PEAK" algorithm, i.e., the line widths are measured at a flux level of 20% of the peak line flux. In order to make our results comparable to PT's result, we converted our 0.5 MEAN line widths to the 0.2 PEAK line widths using the relation $\log w(0.2\ \text{PEAK}) = 0.980 \log w(0.5\ \text{MEAN}) + 0.016$. This empirical relation was found by applying both algorithms to the H I spectra of 100 Sc galaxies. It is reliable for line widths larger than 100 km s^{-1}. These computed 0.2 PEAK line widths should be equivalent to measured 0.2 PEAK line widths, but we expect the random error to be smaller than for directly measured 0.2 PEAK line widths.

The measured line widths were then corrected to edge-on values in the rest frame of the galaxy, $w_i = w(0.2\ \text{PEAK})/[(1 + z) \sin i]$, and finally, rotational velocities w_i^r were derived following the recipes of Tully & Fouqué (1985). The errors in the derived rotational velocities were estimated by quadratically adding the contribution of the uncertainty in the line width as estimated by Bicay & Giovanelli (1986) and the contribution of the uncertainty in inclination. The latter contribution is the larger one in all but the most edge-on galaxies.

The apparent magnitudes were corrected for galactic and internal extinction. Where available we used the galactic H I column density and the Lick survey galaxy counts to compute the former as suggested by Burstein & Heiles (1978); otherwise they were estimated from the galactic latitude b with $\Delta m_{\text{abs}} = 0.25(\cos b - 1)$. Next, we corrected the observed magnitudes to face-on values by estimating the inclination dependent absorption within the galaxy itself using Tully & Fouqué's model of the dust distribution. We used 44% of this predicted value as the absorption for our I magnitudes.

Finally, the magnitudes were corrected for the effect that the bandpass as seen from the rest frame of the galaxy is shifted to the blue for galaxies at higher redshifts. In order to apply this correction, the spectrum must be known in the wavelength range of the I bandpass. The spectral index between 7000 and 8000 Å for Scd galaxies is about -1.34 (Pence 1976). Assuming the same index in the I bandpass, the k-correction amounts to 0.016 mag for galaxies at a redshift of 10,000 km s^{-1}. This small k-correction was also applied to the magnitudes.

We estimated the errors in the total magnitudes by quadratically adding the error estimates of the apparent magnitudes as given in Table 1, the uncertainty in the redshift estimated as suggested by Bicay & Giovanelli (1986), and an assumed random motion of 300 km s^{-1}.

Ultimately, we want to base our magnitudes on PT's calibration and slope of the TF relation. However, PT's sample is based on different selection criteria. Therefore the absolute blue magnitude cutoff described in § 3 was imposed on PT's Virgo sample, and the slope was refitted. A total of 13 galaxies in PT's sample are within this magnitude range. Because of the *absolute* magnitude cutoff, the fit was performed on the inverse TF relation, i.e., the errors were assumed to be in the line widths. This approach also avoids Malmquist bias in the derived distances (Schechter 1980). The resulting value for the slope was -7.93 ± 0.29. This is almost exactly the same value for the slope as the one PT adopted. This indicates that the derived slope is close to the true slope of the TF relation.

To compute peculiar velocities, one still needs to define an expansion rate of the universe relative to which the peculiar velocities are measured. It has been common in recent work to base the expansion rate on the corrected velocity of the Coma Cluster (Lynden-Bell et al. 1988; Willick 1990). We computed the Hubble constant corresponding to an unperturbed velocity at the distance of the Coma Cluster v_{Coma} of 7550 km s^{-1} (Willick 1990) using Aaronson et al.'s (1986) relative distances of Coma and Virgo Cluster. The corresponding Hubble constant is then

$$H = v_{\text{Coma}} \left(\frac{d_{\text{Virgo}}}{d_{\text{Coma}}} \right)_{\text{AA}} / d_{\text{Virgo}} = 85.6 \text{ km s}^{-1} \text{ Mpc}^{-1} , \quad (3)$$

where the d's are distances, the subscript AA denotes values taken from Aaronson et al. (1986), and d_{Virgo} is taken from PT. If the Ursa Major cluster had been used instead of the Virgo Cluster, the value of the Hubble constant would have been the same because the relative distances between Virgo and Ursa Major are the same in PT and Aaronson et al. If the relative distances of Coma and Virgo determined form the D_n-σ relation by Dressler (1987) had been used, the Hubble constant would be about 1% larger.

Figure 5 shows the TF relation of the galaxies listed in Table 1. The absolute magnitudes are computed from redshift velocities in the rest frame of the cosmic microwave background (Lubin et al. 1985) with a Hubble constant as above. The straight line is the fit to PT's sample as described above. If the Hubble constant is adjusted so that the scatter in Figure 5 is minimized, a value of $H = 81$ km s^{-1} Mpc^{-1} and a scatter of 0.41 mag are found.

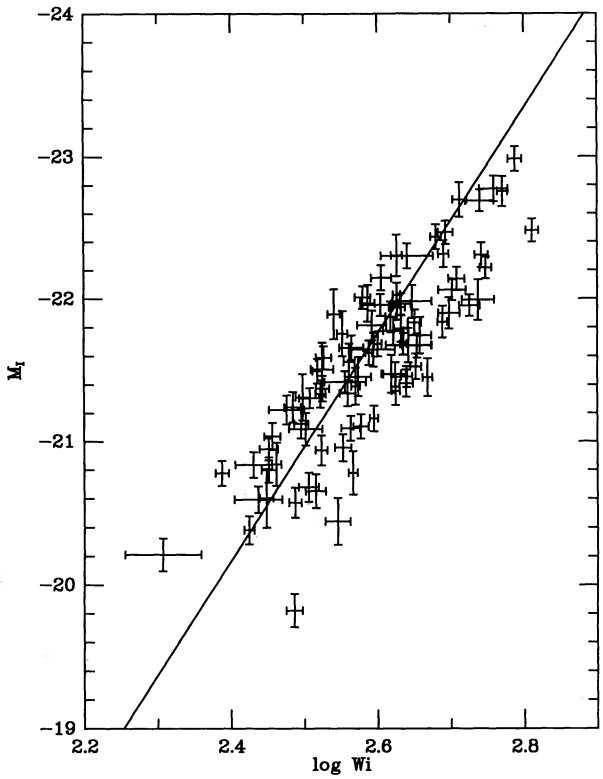

FIG. 5.—The absolute I-band CCD magnitudes vs. the inclination-corrected rotational velocity. The absolute magnitudes were computed with redshift distances and a Hubble constant of $H = 85.6$. The solid line is the Tully-Fisher relation as found by Pierce & Tully 1988.

6. PECULIAR VELOCITIES

The radial component of the peculiar velocity v_{TF} has been computed from the measured redshifts in the frame of the cosmic microwave background v_{CMB} (Lubin et al. 1985) and the measured total magnitudes m_I via

$$v_{TF} = v_{CMB} - 10^{0.2[m_I - (a + b \log w_i') - 15 + 5 \log (H/100)]}, \quad (4)$$

where a and b are the slope and zero point of the TF relation. It should be pointed out that these peculiar velocities are independent of the zero point for the TF relation and therefore of the Hubble constant. It is, however, dependent on the assumed unperturbed redshift velocity of the Coma Cluster.

There are two separate effects which bias distances and therefore peculiar velocities measured with the TF relation. The first is caused by the variation of the number of galaxies with distance; the second is caused by the variation of the number of galaxies with absolute magnitude. The former, often referred to as the Malmquist bias, can be corrected if the distribution of galaxies along the line of sight is known (e.g., Lynden-Bell et al. 1988). The correction for the later requires the knowledge of the luminosity function (e.g., Teerikorpi 1984). Bicknell (1991) gives a combined-treatment of both effects. The Malmquist bias is a serious problem for the mapping of the velocity field, because it creates apparent streaming motion toward mass concentrations, similar to the kind of motion we are searching for. It is therefore not enough to correct for the Malmquist bias expected for constant density. Schechter (1980) showed that this problem can be avoided by using the slope for the TF relation derived from the fit to the inverse relation. Therefore we derived the slope in that way, as described in detail in § 5. The second bias depends on the absolute magnitudes and is therefore distance dependent in a magnitude-limited sample. In such a sample it therefore creates an apparent increase of the derived Hubble constant with distance (e.g., Bottinelli et al. 1988). This problem is avoided by our selection of the sample. Because the range of absolute magnitudes in our sample is independent of distance, no distance dependence of the bias is introduced. There is still some bias for individual galaxies. Because the used range of absolute magnitudes is small, this bias is similar for all galaxies. Furthermore, because the absolute magnitudes are randomly distributed in our sample, the effect of this bias is to add noise to our peculiar velocities rather than to introduce a nonreal streaming motion. The difference in the bias for the brightest and faintest galaxies in our 1.5 mag magnitude range is according to Bicknell (1991) on the order of 3% in distance. The rms noise added to the uncertainty in distance by the bias is therefore less than 1.5%, i.e., much less than the uncertainty due to the intrinsic scatter in the TF relation (see below).

The measured scatter in the TF relation is 0.41 mag. This corresponds to a 1 σ uncertainty in distance of 21%. There are five contribution to this scatter: the error in the measurements of magnitude, inclination, and line width, the random and systematic components of the peculiar motion, possible spotty galactic extinction, the bias as discussed above, and the intrinsic scatter in the relation. The errors in the measurements as listed in Table 1 contribute about 0.05 mag to the scatter. Assuming a rms of 300 km s^{-1} for the random component of the peculiar velocities (Davis & Peebles 1983; de Lapparent, Geller, & Huchra 1988) and a streaming motion as discussed in § 7, the total contribution of the peculiar motion of galaxies to the measured scatter is less than 0.02 mag. While it is difficult to assess the amount of scatter introduced by extinction beyond the one taken into account by the extinction correction describe in § 5, we believe that it is small because there is no dependence of the scatter on the galactic latitude. The largest contribution to the total scatter is therefore the intrinsic scatter in the TF relation. PT suggest that the contribution of the latter is about 0.3 mag or 15% in distance for the Virgo and Ursa Major clusters. While Bothun & Mould (1987) find a similar low scatter for their cluster sample, they find a higher scatter of 0.45 mag for their field sample. The scatter of 0.41 mag in our sample is therefore within the range found by other workers. This scatter translates into an accuracy of about 20% in the derived distances. The expected errors in the peculiar velocity of a single galaxy at the distance of the Hercules supercluster are therefore about 2000 km s^{-1}. This error is significantly larger than the expected infall motion into the Hercules supercluster (see § 7). Only by considering a sufficiently large number of galaxies can we hope to detect such an infall motion.

The resulting peculiar velocities are plotted as a function of redshift in Figure 6. The increase of the errors with distance is clearly visible. Also shown are the averages within each 2000 km s^{-1} redshift bin and the uncertainty within each bin. It can clearly be seen that there is no systematic trend of the peculiar velocity as a function of redshift and therefore no systematic increase or decrease of the Hubble constant as it is seen for closer distances (Tully 1988). The plot also shows that there is no detectable distance dependent bias. We believe that this is a result of the careful selection of the sample. Notice that Malmquist bias does not play a role in the plot of redshift versus peculiar velocities. The average velocity in the bin between 6000 and 8000 km s^{-1} is positive. This is some indication of a possible infall motion into the Hercules supercluster which is located in the next higher velocity bin. In § 8 we will argue that this possible detection of streaming motion is marginally significant.

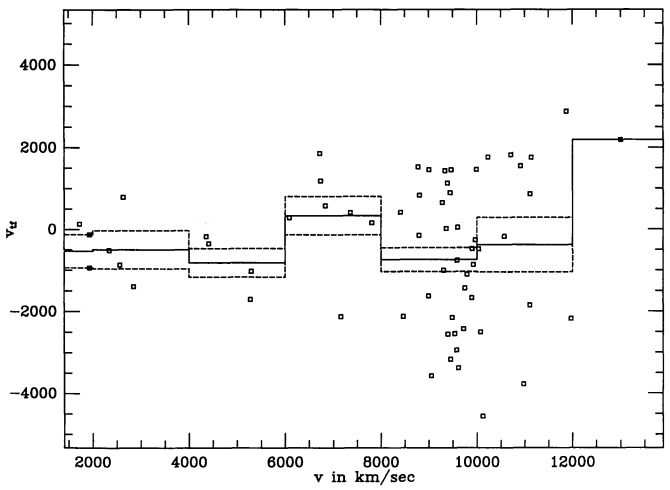

FIG. 6.—Peculiar velocities as computed from the Tully-Fisher relation as a function of redshift. The average of the peculiar velocity and its uncertainty is shown in each redshift bin of 2000 km s^{-1}. The dashed lines indicate the scatter in each redshift bin divided by the square root of the number of galaxies in the bin. There is some indication of infall into the Hercules supercluster at a redshift of about 10,000 km s^{-1}.

7. EXPECTED STREAMING MOTION

In this section, we investigate the expected peculiar velocities in the Hercules region. We assume that all velocities are gravitationally induced. In that case, the velocities are related to the density distribution. Our only knowledge of the density distribution comes from the observed galaxies in the region. While the goal of this section is to model the velocity of the 86 galaxies for which we have measured peculiar velocities, those galaxies by themselves provide only a very incomplete sampling of the distribution of galaxies in space. Therefore, for our model we use all 2165 galaxies with measured redshifts. This sample was described in § 2. The redshift will turn out to be sufficient information to predict peculiar velocities. Linear perturbation theory provides the means to decompose the redshift in a Hubble velocity proportional to the distance and a gravitationally induced peculiar velocity. The only further assumption in the model is that the optically selected galaxies trace mass.

Since the exact value of the Hubble constant is not known and is not needed for the measurement or modeling of peculiar velocities, it is set to unity and dropped from all formulae hereafter. Distances and velocities are therefore measured in km s^{-1} in the physical world and in mesh spacings of a grid (see below) in the computational world. The measured radial velocities of the galaxies relate then to their positions and peculiar velocities as

$$V_i = r_i + \boldsymbol{u}_i \cdot \hat{\boldsymbol{r}}_i \,, \tag{5}$$

where V is the measured radial velocity, r is the distance from the Sun, $\boldsymbol{u}$ is the peculiar velocity vector, and $\hat{\boldsymbol{r}}$ is the unit vector pointing from the observer along the line of sight. The subscripts label individual galaxies.

Linear theory predicts that the peculiar velocity of any given galaxy is

$$\boldsymbol{u}_i \approx \frac{2\boldsymbol{g}_i}{3\Omega^{0.4}} \,, \tag{6}$$

where $\boldsymbol{g}$ is the peculiar acceleration of the galaxy, which depends upon the positions $\boldsymbol{r}_i$ of all galaxies within the horizon. If the peculiar acceleration $\boldsymbol{g}$ of each galaxy is computed from some initial assumption of the distribution of galaxies, the peculiar velocity $\boldsymbol{u}$ can be computed from equation (6) and be fed back into equation (5) to improve the estimates of the positions for the galaxies with measured redshift V_i iteratively. In principle, for a given set of galaxy redshifts and density parameter Ω, a peculiar velocity can be found for every galaxy with a measured redshift. The detailed method is described in § 7.1.

There are two situations in which the iterative approach as outlined above fails to yield an estimate of the peculiar velocity of a galaxy. The first situation is encountered in virialized (or nearly virialized) clusters. There is no unique relationship between the peculiar velocity of a galaxy and its position in a cluster. Clusters were therefore treated as individual entities which is described in detail in § 7.2. The second situation are high mass concentrations, which are not virialized but have a large enough density to make the distance-redshift relation turn over close to the mass concentration. In that case the distance information given by the redshift alone is ambiguous, and those high-density regions have to be treated separately, too. This situation occurs in the Hercules supercluster for high enough Ω, and its treatment is described in § 7.3. In both cases the special treatment is an attempt to place the involved galaxies at a position where their gravitational pull on field galaxies is realistic. However, for the galaxies in the special regions themselves we cannot estimate any unique peculiar velocity.

7.1. *Peculiar Accelerations*

The total acceleration $\boldsymbol{g}_i$ on the ith galaxy can formally be split into the sum of the acceleration caused by all field galaxies, and the sum of the accelerations from clusters,

$$\boldsymbol{g}_i = \sum_{j \neq i}^{N} \boldsymbol{g}_{ij} + \sum_{k}^{N_C} \boldsymbol{g}_{ki}^{C} \,, \tag{7}$$

where the first term is the acceleration due to the $N - 1$ other field galaxies; the second term is the acceleration due to the N_C clusters. The gravitational acceleration due to the clusters is discussed in § 7.2.

Of course the positions or masses of all the galaxies within the horizon are not known, and our knowledge from limited redshift samples has to be used to approximate the distribution of galaxies. For the volume covered by the above described redshift sample, one could simply sum over the accelerations from all galaxies in the sample giving each galaxy a proper weight (see Strauss & Davis 1988). However, since we do not have a volume-limited sample of galaxies, it is desirable to smooth the density distribution of galaxies. This smoothing is especially important for larger distances where the sampling becomes sparser and where the shot noise increases rapidly if direct summation is used. Smoothing is also important in high-density regions where galaxies that are close in space will be assigned a high peculiar acceleration and therefore, in linear theory, a high peculiar velocity if direct summation is used. In order to balance the desired needs for efficiency, dynamic range, and resolution, a particle-mesh code (hereafter PM code; see Hockney & Eastwood 1980, hereafter HE, for details) was used to compute the peculiar acceleration caused by the field galaxies. The estimated positions $\boldsymbol{r}_i$ of the galaxies were used to compute the density field ρ on a cubic grid and evaluate the gravitational potential ϕ by solving Poisson's equation on the grid with a Fourier transform method. The potential was then differentiated to get the acceleration field on the grid and interpolated at the galaxy positions.

The Fourier solution to the Poisson equation imposes periodic boundary conditions. To minimize the interaction of galaxies with the mirror images, a total grid size of 64^3 was used, and a scale of 400 km s^{-1} per mesh spacing was used to assign physical positions to the grid. With this scale, the complete redshift sample was contained within one octant of the grid, and therefore the whole sample well separated from the mirror images. The choice of unity for the Hubble constant and the scale of the cube in grid spacings per redshift define the computational units. The selection of an Ω then fixes the mass scale and the gravitational constant G in computational units can be computed from the definition of Ω and the average density within the sampled cone. This choice of G implicitly converts the measured number density into a mass density.

The density at the grid points was computed using the standard *Triangular Shaped Cloud* (TSC) assignment scheme (HE) for all galaxies but those located in the Hercules supercluster (see § 7.3). The TSC scheme distributes the mass of each galaxies onto 3^3 grid points. The "mass" of each particle was set to the weight as described in § 2. The mass of all particles was

then added up, and the total mass was used to compute the average density within the sampled cone. The gravitational constant G was then computed as described above.

Some assumption has to be made about the density distribution outside the sampled cone. The simplest assumption is that the unsampled regions have a uniform density equal to the mean density inside the sampled cone. Technically, this is implemented by subtracting the average density from all grid points inside the sampled cone and setting the density on grid points in the unsampled region to zero. We used this assumption but noted that from limited redshift surveys we know about the Bootes void close behind the sampled cone. Because of its size and proximity to the Hercules region, the Bootes void influences some of the dynamics of the galaxies at higher redshifts in the cone, i.e., galaxies located in the Hercules supercluster. We treated the Bootes void as a perfect sphere located at $\alpha = 14^h20^m$, $\delta = 46°$, $r = 15{,}500$ km s^{-1} with a radius of 3100 km s^{-1} and a density of 10% of the background density inside the void (Kirshner et al. 1987). A perfect sphere outside the sampled cone acts exactly like a point mass. Its negative mass in computational units can be computed from $M_{\rm Bootes} = \rho_b V$, where V is the volume of the void. We do not include this void in the computation of the background density, because we assume that the Bootes void is not typical and that the density within our cone might be a more accurate representation of the average density of the universe. In fact, this assumption cannot be tested until much deeper redshift surveys of the local universe are available. In other respects, we treat the void like one of the clusters (see § 7.2) but with a negative mass. The effect of the Bootes void is to increase the infall velocity into the Hercules supercluster of galaxies located behind the supercluster. For example, with $\Omega = 1$, the Bootes void contributes about 300 km s^{-1} to the peculiar velocity of a galaxy with a redshift of 10,000 km s^{-1} and a projected position in the sky right on top of the void. Figure 7 shows a projection of the computational volume, with the sample wedged in the bottom left-hand corner. The clusters and the Bootes void are also indicated. The resolution of the grid is shown in the upper right-hand corner.

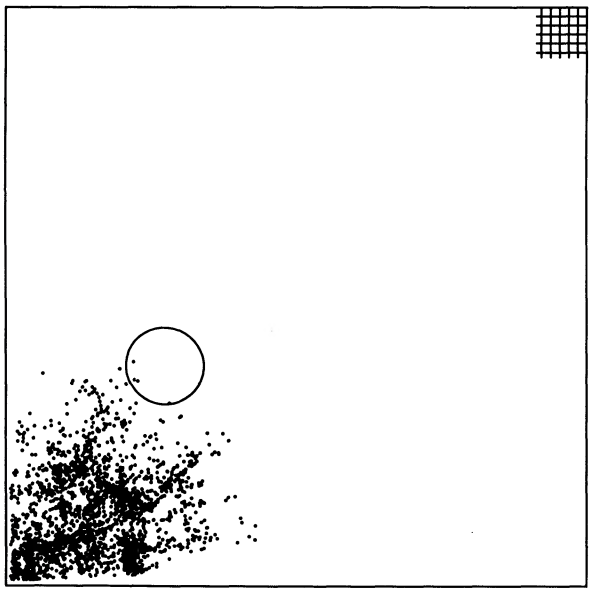

FIG. 7.—Position of the galaxies in the modeled cube. Small dots represent galaxies and large point clusters of galaxies, and the circle represents the Bootes void. All positions are projected into one plane. The whole modeled region occupies only a small fraction of the cube so that forces from the mirror images are small. The grid spacing and therefore the smoothing length is indicated by the grid in the upper right corner.

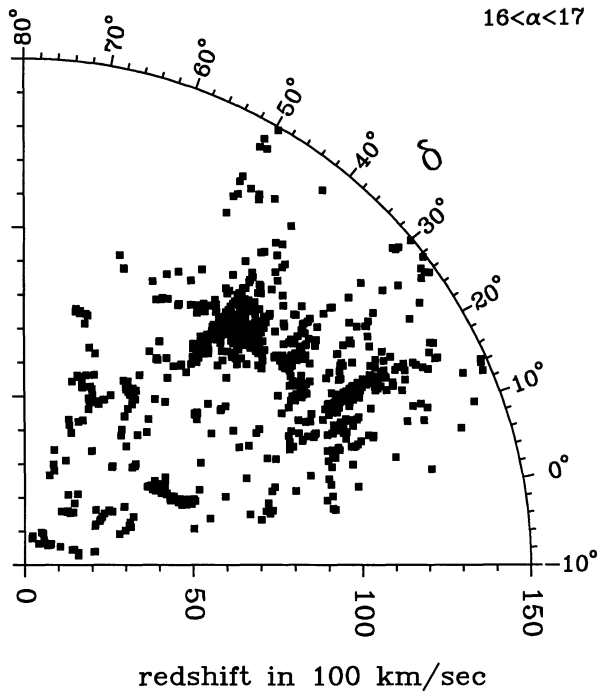

FIG. 8.—The distribution of galaxies in the redshift sample in one slice through the Hercules region. Shown is the slice with $16^h \leq \alpha \leq 17^h$.

7.2. *Clusters in the Hercules Region*

The most obvious deviations from a smooth Hubble flow in the Hercules region are the "fingers of God" produced by the rich clusters in the region (see Fig. 8). Because the density in the core of the clusters is high and the clusters themselves are overdensities typically of contrast much larger than unity, linear theory does not apply. The crossing times in the clusters are about 5% of a Hubble time (Tarenghi et al. 1980); therefore the relationship between distances and redshift is lost because the galaxy crossed the cluster many times. Cluster galaxies were therefore removed from the sample before computing the density field on the grid. Table 2 lists the clusters present in our sample and gives the redshifts and velocity dispersions σ (Struble & Rood 1987) and apparent radii r_c (Leir & van den Bergh 1977). All galaxies within two cluster radii r_c of any cluster with velocity dispersion estimates σ as listed in Table 2 and within 1.5 σ of the radial velocity of this cluster were assumed to be cluster members and were removed from the galaxy sample. Figure 9 shows the same slice as Figure 8, but with the clusters removed. It can be seen that the "Fingers of God" were successfully removed without much impact on the surroundings of the clusters.

In order to account for their overall contribution to the local overdensity, the clusters removed in this manner can be incorporated into the density profile by replacing them with a single particle at the position of the cluster center. The weight assigned to the individual clusters can be determined in one of several ways. In the simplest case, the weight might be equal to the added weights of the individual galaxies, computed with the

TABLE 2

CLUSTER PROPERTIES

Cluster	α (1950)	δ (1950)	cz (km s^{-1})	σ (km s^{-1})	n[a]	r_c	M_{vt} (10^{14} $M_\odot$)	M_{vt}/M_{est}
A1983.....	$14^h50^m.4$	+16°57′	13221	433	8	48′	5.7	1[b]
A2052.....	15 14.3	+7 00	10433	576	37	22	3.7	1[b]
A2063.....	15 20.6	+8 49	10103	521	21	39	5.1	1[b]
A2147.....	16 00.0	+16 02	10672	1148	30	56	26.8[c]	0.70
A2151.....	16 03.0	+17 53	11122	887	42	28	11.8[c]	0.96
A2152.....	16 03.1	+16 35	11212	1244	22	28	34.5[c]	1.46
A2197.....	16 26.5	+41 01	9234	593	46	50	7.5[d]	0.94
A2199.....	16 26.9	+39 38	9264	807	70	45	13.8[d]	0.94

[a] Number of galaxies used by Struble & Rood 1987 to determine cz and σ.
[b] Assumed to be 1.
[c] From Tarenghi et al. 1980 transformed to $H_0 = 75$ km s^{-1} Mpc^{-1}.
[d] Computed from harmonic mean separations given by Gregory & Thompson 1984.

assumption that the galaxies are all located at the distance of the cluster center. However, this approach has several disadvantages:

1. Using the weights of the galaxies as a direct indicator of mass assumes a constant light-to-mass ratio. The light-to-mass ratio is known to be different from cluster to cluster (e.g., Tarenghi et al. 1980) and might be very different in the rest of the supercluster.

2. The redshift samples of galaxies in clusters are selected in a fundamentally different way than redshift samples of field galaxies. Most cluster redshifts were obtained in the course of detailed surveys of particular clusters that often extend much deeper than the CGCG catalog. The computed weights for cluster galaxies may therefore be systematically different from those computed for field galaxies.

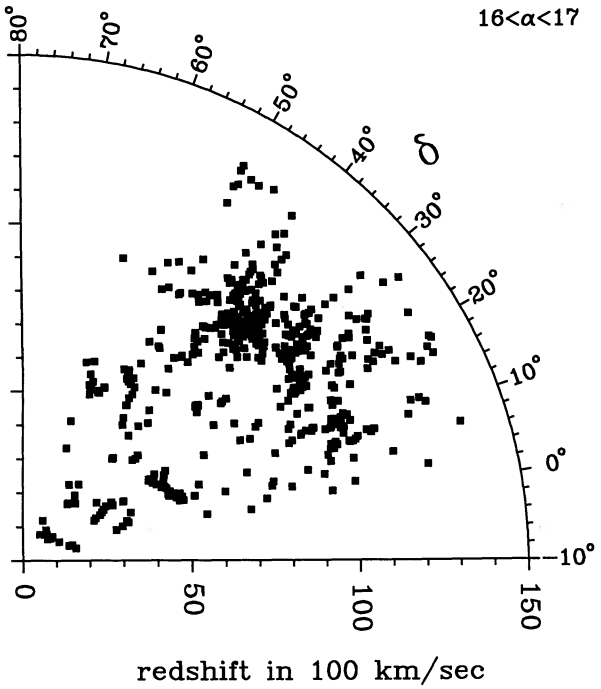

FIG. 9.—Same as Fig. 8, but clusters removed

3. The computed weights would not use the information on cluster masses also available from the velocity dispersions in the clusters.

We therefore used estimates of the virial mass of the clusters to compute the expected velocities in the Hercules region. These estimates do not depend on Ω and are therefore the same for all models. In fact, for high values of Ω, the virial masses of the clusters do not significantly contribute to the density distribution. The mass of the clusters can be estimated from their velocity dispersion,

$$M_{vt,k} = \frac{2\pi\sigma_k^2 r_{h,k}}{G}, \tag{8}$$

where r_h is the mean harmonic separation, σ is the velocity dispersion in the cluster, G is the gravitational constant, and the subscript k labels individual clusters. Even though some clusters, in particular the Hercules cluster A2151, are clearly not isotropic, this formula can be used to obtain a rough estimate of the cluster masses.

Virial masses for the five major clusters are taken from the literature. The masses for A2147, A2151, and A2152 were given by Tarenghi et al. (1980). The masses for A2197 and A2199 given by Gregory & Thompson (1984) were recomputed using their value of the harmonic mean separation within one Abell radius, but using the velocity dispersion computed from their data by Struble & Rood (1987). The resulting masses are listed in Table 2, for a Hubble constant of $H = 75$ km s^{-1} Mpc^{-1}. We also computed mass estimates from global cluster properties with

$$M_{est} = \text{const} \times \sigma^2 r_c\, cz, \tag{9}$$

where σ and r_c are the velocity dispersion and angular radius of the cluster as listed in Table 2, and the "const" has been adjusted so that the average of M_{est} of the five clusters is identical to the average of M_{vt}. The ratio M_{est}/M_{vt} for each cluster is listed in the last column of Table 2. Its scatter is 28% so that M_{est} seems to be suitable as a rough estimate of the virial mass. The virial mass for the three less massive clusters with velocity dispersion in Table 2 has therefore been set to M_{est}.

The acceleration of galaxies due to the clusters at position $\boldsymbol{R}_k$,

$$\boldsymbol{g}_{ki}^C = \frac{GM_k(\boldsymbol{R}_k - \boldsymbol{r}_i)}{|\boldsymbol{R}_k - \boldsymbol{r}_i|^3}, \tag{10}$$

is then just added to the peculiar acceleration of each galaxy as indicated in equation (7).

7.3. *The Triple Value Region*

A strong mass concentration can generate velocities large enough so that for some lines of sight close to the mass concentration, the redshift as a function of velocity decreases, i.e. in such a region galaxies with higher redshift are closer than those with lower redshift. The solid line in Figure 10 illustrates this situation. In such a region, in general three different distances correspond to a given measured redshift. A well-known example of such a *Triple Value Region* (TVR hereafter) in the local universe is the Virgo Cluster (Tonry & Davis 1981). The density contrast in the Hercules supercluster creates the same effect. It is not possible to infer a distance for a galaxy in TVRs from the measured redshift alone, and therefore the peculiar velocity from the model is ambiguous. Therefore such galaxies were excluded from the comparison of measured and modeled velocities in § 7. However, because of their gravitational interaction with other galaxies, it is necessary to decide where to put those galaxies in the model. This decision is necessary even for those few galaxies for which we have redshift-independent TF distances, because the TF distances are not accurate enough to resolve this ambiguity. The detailed density distribution within the TVR is only a second-order effect on the peculiar acceleration of the galaxies outside that region. It is therefore only necessary to identify galaxies in a triple value region and set them at the right distance of the density enhancement, in our case the Hercules supercluster. Of course the true distance of the supercluster is not known, so we assume that its peculiar velocity is zero (see Fig. 10).

The identification of the galaxies in TVRs was done by computing the velocity-distance relation from linear theory along the line of sight of each galaxy. The distance for galaxies within a TVR was then set to the distance at which the peculiar velocity as computed from linear theory was zero. If the distances of all galaxies in the TVR were set exactly to that distance, a very high density region would be created and the peculiar velocities as computed from linear theory would be very high. In the next iteration, the TVR would therefore grow, and more galaxies would be assigned to the supercluster. In practice, the PM algorithm as described above already distributes the mass of each particle onto 27 mesh points ($3 \times 3 \times 3$), therefore naturally spreading the particles and avoiding computed peculiar velocities which are too high. Still, we found that in order to avoid too high a mass concentration, it is advantageous to replace the TSC assignment scheme by the higher order *Piecewise Cubic Spline* assignment scheme (PSC) for galaxies in the TVR region only. For details on the PSC scheme see Monaghan (1985), but note the missing binomial coefficients in his equation (3.8). That scheme distributes the mass of each particle on 125 mesh points ($5 \times 5 \times 5$), thus significantly increasing the spreading. The resulting TVR is roughly in agreement with a subjective outline of the supercluster in redshift space.

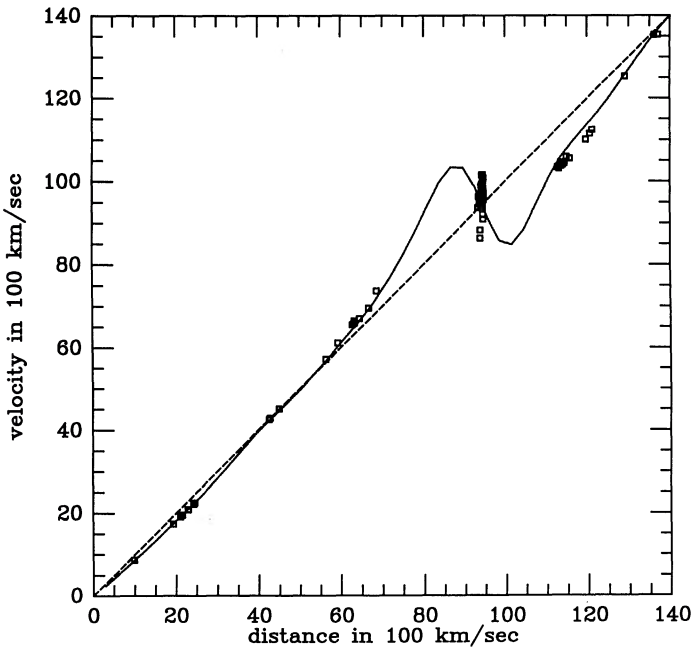

FIG. 10.—The distance-velocity relation for galaxies in a 5° cone around UGC 10019. The solid line represents the relation as computed from the linear theory with a density parameter of $\Omega = 1$, and the dashed line is the relation with no peculiar velocities. The squares represent the positions which were actually determined by the program. Note the treatment of the particles in the triple value region.

7.4. *Limitations of the Model*

The major limitations of the model are the small angular size and the limited depth of the redshift survey. The impact of the limited survey volume is twofold. In defining the value of the density parameter Ω, we need to assume that the sampled volume is a fair sample of the universe. De Lapparent et al. (1988) showed that the average density as determined from the CfA redshift slice had an uncertainty of about 25%. The uncertainty in our cone is somewhat higher because only a subvolume is sampled as deeply as the CfA slice. A 25% uncertainty results in an uncertainty of 45% in the density parameter Ω.

In addition, the finite sample volume forces us to make assumptions about the distribution of galaxies outside the surveyed cone. In the absence of additional information about the density distribution outside the Bootes void, we had to approximate it as a homogeneous distribution. The impact of this approximation on the computed velocities is more difficult to estimate. Strauss & Davis (1988) computed the peculiar acceleration vector on the Local Group from the distribution of galaxies detected by *IRAS*. They find that the acceleration converges when a region with a radius of 3400 km s^{-1} is used. If we assume this situation to be typical, we might hope that the region we sample is large enough to compute accurately the present gravitational acceleration on galaxies around the Hercules void, especially on those galaxies located on the near side of the void at a redshift of about 5000 km s^{-1}. The front side of the void is especially important because the distance estimates and therefore the measured velocities are more accurate at lower redshifts.

8. COMPARISON WITH OBSERVED VELOCITIES

With the above caveats, it is nonetheless valuable to compare the expected and observed velocities. We computed the expected velocities for the cases $\Omega = 1$ and $\Omega = 0.5$. Galaxies in the above described cone ($14^h \leq \alpha$, $2°.5 \leq \delta \leq 62°.5$ and $b \geq 40°$ and redshifts corrected to the rest frame of the cosmic microwave background of less than 14,000 km s^{-1}) with magnitudes brighter than 15.7 were used to estimate the matter distribution.

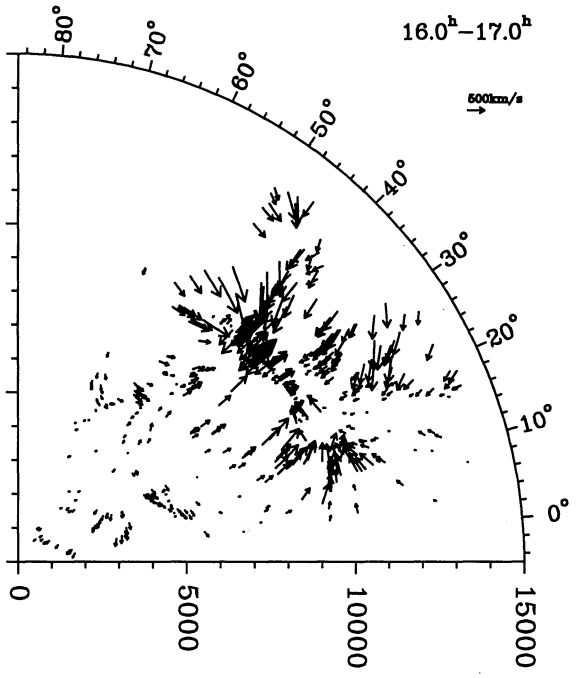

FIG. 11.—Predicted velocity field for the galaxies in the same slice as in Fig. 8. The velocity vectors are projected onto the plane in the center of the slice.

The iterative computation of the peculiar velocities converged within six steps to a rms of less than 20 km s^{-1} for $\Omega = 1$. As an example for the resulting velocity field, we show in Figure 11 velocity vectors for $\Omega = 1$ for galaxies in one slice through the Hercules region, namely the same slice as shown in Figure 8. The velocity vectors are projected onto the plane in the center of the slice. The expansion of the void can easily be recognized. The motion outward from the center of the void is about 300 km s^{-1}. However, the main dynamical feature is the Hercules supercluster. Inwards motions up to 600 km s^{-1} are shown. The predicted velocities of galaxies are influenced by the assumption that the distribution of galaxies is smooth outside of the cone defined above. This assumption affects galaxies close to the edge of this cone more than galaxies close to the center of the cone. The infall of galaxies at the edge of the cone into the Hercules supercluster is probably an artifact of this assumption, because we know that the supercluster extends further than the cone.

A different representation of the velocity field is shown in Figure 10, which shows the expected streaming motion along the line of sight of UGC 10019. This plot also illustrates the treatment of galaxies in the TVR. The turnaround radius of the Hercules supercluster is about 600 km s^{-1} in redshift space for $\Omega = 1$. Since the supercluster is part of the larger "Great Wall," a region with similar turnaround radius would surround us if Ω is high.

The measured peculiar velocities of the 65 galaxies of the TF sample located in the modeled cone was compared to the modeled velocities. Ten of those galaxies are fainter than 15.7 mag. These galaxies do not contribute to the density profile, because we have no way to estimate the completeness of faint galaxies and therefore cannot assign a weight to them. Their weight has been set to zero. The estimated peculiar velocities are of course independent of the mass of the particle; those faint galaxies behave therefore like test particles in an external field. The velocities computed with a density parameter of $\Omega = 1$ are higher than the peculiar measured peculiar velocities as indicated in Figure 6. Figure 12*a* shows the peculiar radial velocities as a function of distance for the galaxies in the TF sample computed with $\Omega = 0.5$. In Figure 12*b* the measured peculiar velocities are shown for the same galaxies. The distances in both Figures 12*a* and 12*b* are computed from the redshift and the peculiar velocities from the model. Both figures show superposed the least-squares fit of a fifth-order polynomial. Both parts of the figure show some signs of infall of galaxies into the Hercules supercluster. The value $\Omega = 0.5$ was chosen to adjust the amplitude of this infall in the model to the measured infall. The polynomial fit in Figure 12*b* shows a slight tendency towards negative peculiar velocities for higher

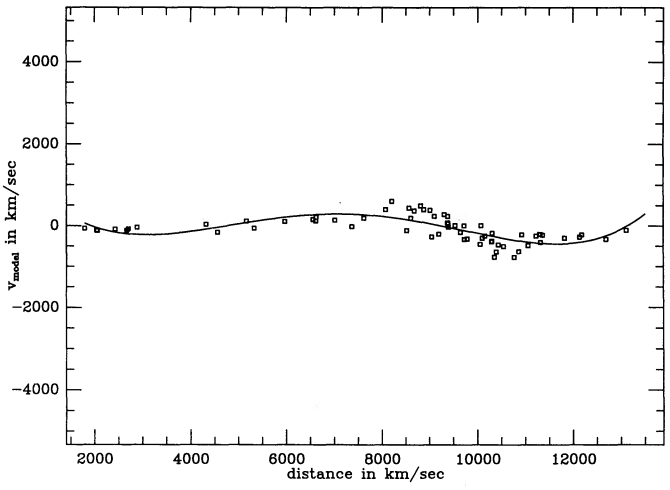

FIG. 12*a*

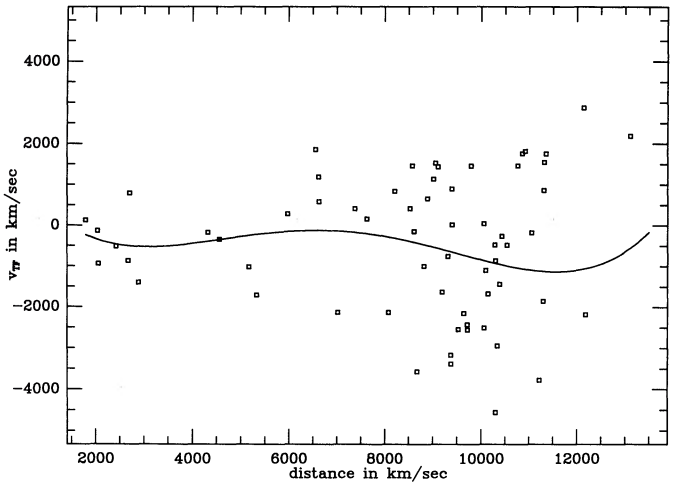

FIG. 12*b*

FIG. 12.—Fig. 12*a* shows the modeled peculiar velocities for $\Omega = 0.5$ as a function of distance, and Fig. 12*b*, the measured peculiar velocities as a function of distance. The distances in both cases are computed as the redshift minus the peculiar velocities as computed from the model. The solid lines in both parts of the figure are fifth-order polynomials obtained from least-squares fits to the points.

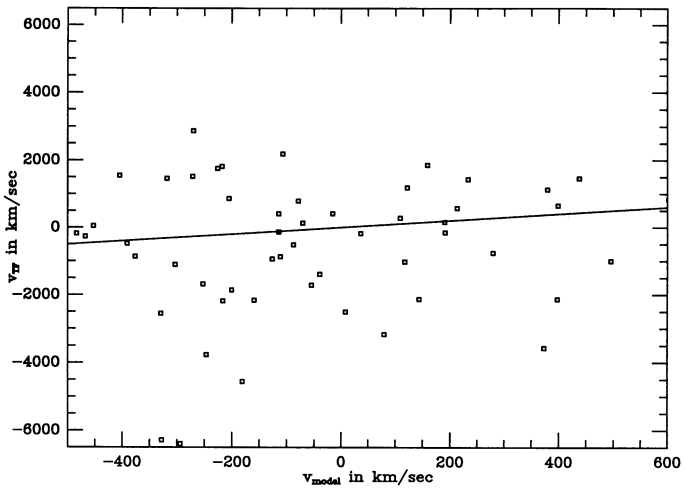

FIG. 13.—Modeled peculiar velocities for $\Omega = 0.5$ vs. measured peculiar velocities. The solid line has a unity slope.

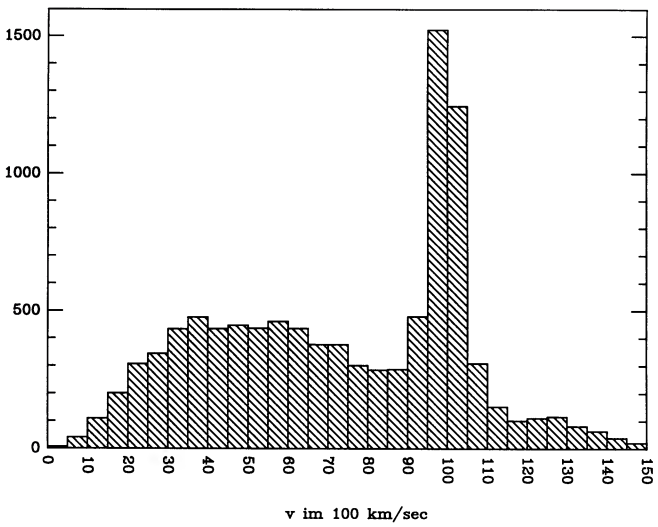

FIG. 14.—Redshift distribution of the galaxies in the Monte Carlo simulation.

distances. One can compensate for this tendency by slightly adjusting the Hubble constant used to compute the measured peculiar velocities. A Hubble constant of $H = 87$ results in an almost perfect alignment of the polynomials in Figures 12*a* and 12*b*. Such a Hubble constant would correspond to a corrected redshift of Coma of 7673 km s^{-1}. The difference with Willick's (1990) value is well within his 1 σ error estimate of 245 km s^{-1}.

Figure 13 compares the radial velocities predicted by the model with those measured with the TF relation. The 12 galaxies of the TF sample located in the TVR are excluded from this plot. A Spearman rank-order correlation coefficient between measured and predicted velocities is only 0.08. If the joint probability distribution of the predicted and measured probability function is binormal, the probability of finding such a correlation in the absence of a true correlation is almost 50%.

The high negative velocities in Figure 13 reflect the predicted infall of galaxies in the Hercules supercluster for galaxies which are located behind the supercluster. At such high redshifts, we expect the predicted velocities to be uncertain because of the sparse sampling at high redshifts. The measured velocity in that region are also the most uncertain because of the high distance of the galaxies involved. This is evident in Figure 13 from the higher scatter. If galaxies with velocities less than -200 km s^{-1} are excluded, the correlation coefficient increases to about 0.27. The probability of finding such a correlation in the absence of a true correlation is about 15%. We therefore conclude that there is a marginally significant correlation between the modeled and observed velocities.

If the density parameter Ω of the universe is the same as the one in the model, a linear relation with unity slope between the measured velocities and the velocities in the model is expected. Our choice of $\Omega = 0.5$ for the model was guided by the comparison of Figures 12*a* and 12*b*. From equation (6) we find that $\boldsymbol{u} \approx \boldsymbol{u}_{0.5}(2\Omega)^{0.6}$, where $\boldsymbol{u}_{0.5}$ is the velocity found for $\Omega = 0.5$. A density parameter Ω slightly different from 0.5 therefore changes to first order the expected relation between measured velocities and modeled velocities to a straight line with a slope different from unity. This is only approximately true because the positions of the galaxies change in models with different Ω. A straight line was fitted to the points shown in Figure 13. The resulting slope is 0.9 ± 0.3. Using the above approximation, we therefore find $\Omega = 0.4^{+0.3}_{-0.2}$. Because of the marginal significance of the correlation, the upper limit of $\Omega \leq 0.7$ should be considered as the most significant result. The zero point of the fit was -390 ± 240 km s^{-1}, which suggests with low significance that the whole Hercules region is moving toward us.

We carried out a Monte Carlo experiment which duplicates the full impact of the various steps in the selection of the sample as described in § 3. The galaxies were given distances randomly drawn from an homogeneous distance distribution with a simulated supercluster at a redshift of 10,000 km s^{-1}. The distance distribution is shown in Figure 14. Subsequently, the galaxies were assigned blue magnitudes randomly drawn from a Gaussian luminosity function with a mean of $M_B = -18.4$ and a dispersion of $\sigma = 1.5$ mag (Binggeli, Sandage, & Tammann 1988), *I*-band magnitudes, and H I line width in accordance with the Tully-Fisher relation with a scatter of 0.40 mag and parameters as discussed in § 5. Finally, the redshifts were created by imposing a Gaussian random peculiar velocity component of 300 km s^{-1} and an infall into the supercluster with an infall velocity of 600 km s^{-1}. From this catalog, galaxies were selected in three steps. First, a magnitude-limited catalog with limiting magnitude of 15.7 was selected. Second, a subsample of this catalog was selected with the completeness of the H I sample (see FHG) imposed. Finally, the same absolute magnitude criteria as used for the real sample was used to select the artificial TF sample. The peculiar velocities were computed from the TF relation of that final sample and compared to the true peculiar velocities. We recovered the true velocities with an accuracy of about 10%.

9. DISCUSSION AND CONCLUSION

The marginal correlation between the modeled and the measured velocities shows that the Hercules is a dynamically relatively quiet region. This is consistent with previous findings that the local velocity field is dominated by the infall into the GA which is in a direction perpendicular to the Hercules region. However, this result is not expected if the high peculiar velocities measured by Lynden-Bell et al. (1988) and Willick (1990) are gravitationally induced.

Strauss & Davis (1988) modeled the expected velocity of *IRAS* galaxies with a characteristic redshift depth of about 4000 km s^{-1} with a model similar to the one we used. Their comparison of the computed velocity field with velocities measured with the D_n-σ relation suggests that the velocities from an $\Omega = 1$ model are too small. The value of Ω derived from those velocities is $\Omega \approx 3$. Comparison of their velocity field with velocities measured with the TF relation seems to be consistent, if less significant, with this high Ω (see their Figs. 8 and 9). The comparison of the computed velocities with the observed velocities in the Hercules region clearly excludes such a high Ω. This difference might be caused by the difference in sampling the matter distribution of *IRAS* galaxies versus our redshift sample. Because *IRAS* galaxies are uniformly selected over large portions of the sky independent of galactic extinction, they should constitute a more accurate estimate of the matter distribution. However, it is unlikely that our estimate of overdensities is off by as much as a factor of 3.3, which would roughly change our estimate of Ω from 0.4 to 3. If the difference in the derived Ω is a true physical result, it might indicate a different level of biasing in the Hercules supercluster compared to the part of universe within a redshift of 4000 km s^{-1}. Recently, Willick (1990) found an outstreaming motion of about 550 km s^{-1} around the void in the Pisces-Perseus region. Since the Pisces-Perseus void is smaller than the Hercules void, this motion is probably also larger than what would be expected if the velocity is induced by gravity in an $\Omega = 1$ universe.

The question whether the velocity field in the local universe is really dominated by large, gravitationally induced streaming remains open so far. At least for the Hercules region, we can state that large peculiar velocities in excess of those expected in an $\Omega = 1$ universe, as have been suggested for other regions, are not present.

This work resulted from the work done by W. F. for a Ph.D. dissertation at Cornell University, which was supervised by M. P. Haynes. We also acknowledge conversations and suggestions by Riccardo Giovanelli, Marc Davis, Luiz DaCosta, and Geoffrey V. Bicknell. The model presented in § 7 was constructed using the Cornell National Supercomputer Facility, a resource of the Cornell Theory Center, which receives major funding from the National Science Foundation and IBM Corporation, with additional support from New York State and members of the Corporate Research Institute.

REFERENCES

Aaronson, M., Bothun, G., Mould, J., Huchra, J., Schommer, R. A., & Cornell, M. E. 1986, ApJ, 302, 536
Bertschinger, E., & Dekel, A. 1989, ApJ, 336, L5
Bicay, M. D., & Giovanelli, R. 1986, AJ, 91, 705
Bicknell, G. V. 1991, preprint
Binggeli, B., Sandage, A., & Tammann, G. A. 1988, ARA&A, 26, 509
Bothun, G. D., & Mould, J. R. 1987, ApJ, 313, 629
Bottinelli, L., Gouguenheim, L., Paturel, G., & Teerikorpi, P. 1988, ApJ, 328, 4
Burstein, D., & Heiles, C. 1978, ApJ, 225, 40
Davis, M., & Peebles, P. J. E. 1983, ApJ, 267, 465
de Lapparent, V., Geller, M. J., & Huchra, J. P. 1986, ApJ, 302, L1
———. 1988, ApJ, 332, 44
———. 1989, ApJ, 343, 1
Dressler, A. 1987, ApJ, 313, 1
Dressler, A., & Faber, S. M. 1990, ApJ, 354, 45
Dressler, A., Lynden-Bell, D., Burstein, D., Davies, R. L., Faber, S. M., Terlevich, R. J., & Wegner, G. 1987, ApJ, 313, 42
Fouqué, P., Bottinelli, L., Gouguenheim, L., & Paturel, G. 1990, ApJ, 349, 1
Freudling, W. 1990, Ph.D. thesis, Cornell University
Freudling, W., Haynes, M. P., & Giovanelli, R. 1988, AJ, 96, 1791 (FHG)
———. 1991, in preparation
Geller, M. J., & Huchra, J. P. 1989, Science, 246, 857
Gregory, S. A., & Thompson, L. A. 1984, ApJ, 286, 422
Gregory, S. A., Tifft, W. G., & Moody, J. W. 1988, AJ, 95, 662
Haynes, M. P., & Giovanelli, R. 1989, private communication
Hockney, R. W., & Eastwood, J. W. 1981, Computer Simulation Using Particles (New York: McGraw-Hill) (HE)
Huchra, J. P. 1989, private communication
Huchra, J. P., Davis, M. M., Latham, D. W., & Tonry, J. L. 1982, ApJS, 52, 89
Jedrzejewski, R. I. 1987, MNRAS, 226, 747
Kirshner, R. P., Oemler, A., Jr., Schechter, P. L., & Shectman, S. A. 1987, ApJ, 314, 493
Leir, S., & van den Bergh, S. 1977, ApJS, 34, 381
Lubin, P., Villela, T., Epstein, G., & Smoot, G. 1985, ApJ, 298, L1
Lynden-Bell, D., Faber, S. M., Burstein, D., Davies, R. L., Dressler, A., Terlevich, R. J., & Wegner, G. 1988, ApJ, 326, 19
Monaghan, J. J. 1985, Comp. Phys. Rep., 3, 71
Nilson, P. 1973, Uppsala General Catalog of Galaxies, Uppsala Astr. Obs. Ann., 6 (UGC)
Pence, W. D. 1976, AJ, 203, 39
Pierce, M. J., & Tully, R. B. 1988, ApJ, 330, 579 (PT)
Schechter, P. L. 1980, ApJ, 85, 801
Schoening, B. 1988, The CCD Direct Imaging Camera No. 1 0.9 Meter Telescope (Kitt Peak National Observatory)
Silk, J. 1989, ApJ, 345, L1
Staveley-Smith, L., & Davies, R. D. 1989, MNRAS, 241, 787
Strauss, M. A., & Davis, M. 1988, in Large Scale Motion in the Universe, ed. V. C. Rubin and G. V. Coyne (Princeton: Princeton Univ. Press), 255
Struble, M. F., & Rood, J. R. 1987, ApJS, 63, 543
Tarenghi, M., Chincarini, G., Rood, H. J., & Thompson, L. A. 1980, ApJ, 235, 724
Teerikorpi, P. 1984, A&A, 141, 407
———. 1990, A&A, 234, 1
Tonry, J. L., & Davis, M. 1981, ApJ, 246, 680
Tully, R. B. 1988, Nature, 334, 209
Tully, R. B., & Fouqué, P. 1985, ApJS, 58, 67
Tully, R. B., & Shaya, E. J. 1984, ApJ, 181, 31
Willick, J. A. 1990, ApJ, 351, L5
Zwicky, F., Herzog, E., Will, P., Karpowicz, M., & Kowal, C. 1961–1968, Catalog of Galaxies and Clusters of Galaxies, 6 vols. (Pasadena: California Institute of Technology) (CGCG)